Figure 57. Row vectors $\mathcal{W}_{n\bullet}^T$ of the discrete wavelet transform matrix $\mathcal{W}$ based on the Haar wavelet for $N = 16$ and $n = 0$ to 7 (top to bottom on left plot) and $n = 8$ to 15 (right plot).
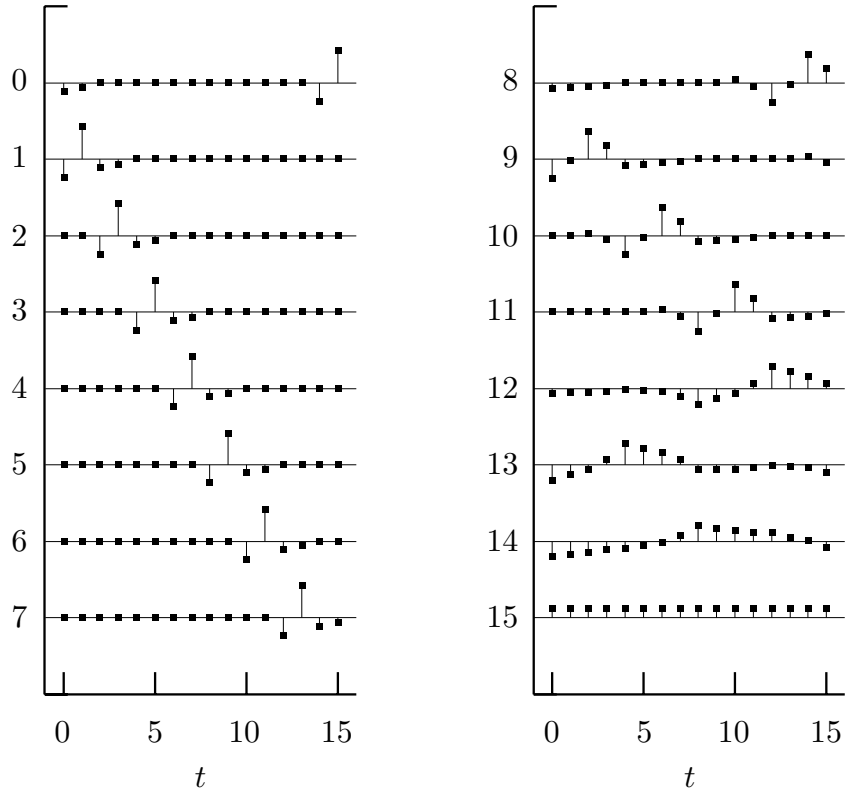
Figure 60. Row vectors $\mathcal{W}_{n\bullet}^T$ of the discrete wavelet transform matrix $\mathcal{W}$ based on the D(4) wavelet for $N = 16$ and $n = 0$ to 7 (top to bottom on left plot) and $n = 8$ to 15 (right plot).
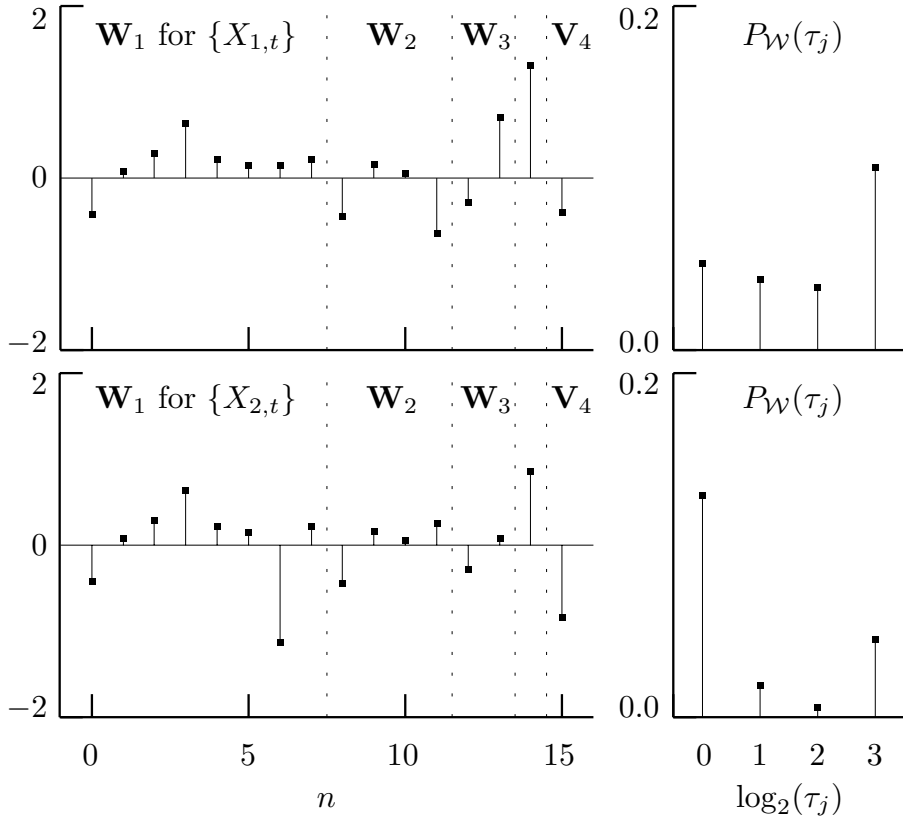
Figure 62. Haar DWTs for the two time series in Figure 42. The DWT coefficients **W** are shown in the left-hand plots (the corresponding discrete wavelet empirical power spectra are in the right-hand plots). The thin dotted lines delineate the subvectors $\mathbf{W}_1$, $\mathbf{W}_2$, $\mathbf{W}_3$, $\mathbf{W}_4$ and $\mathbf{V}_4$ (see Equation (61c); $\mathbf{W}_4$ is between $\mathbf{W}_3$ and $\mathbf{V}_4$ but is unlabeled due to lack of space).
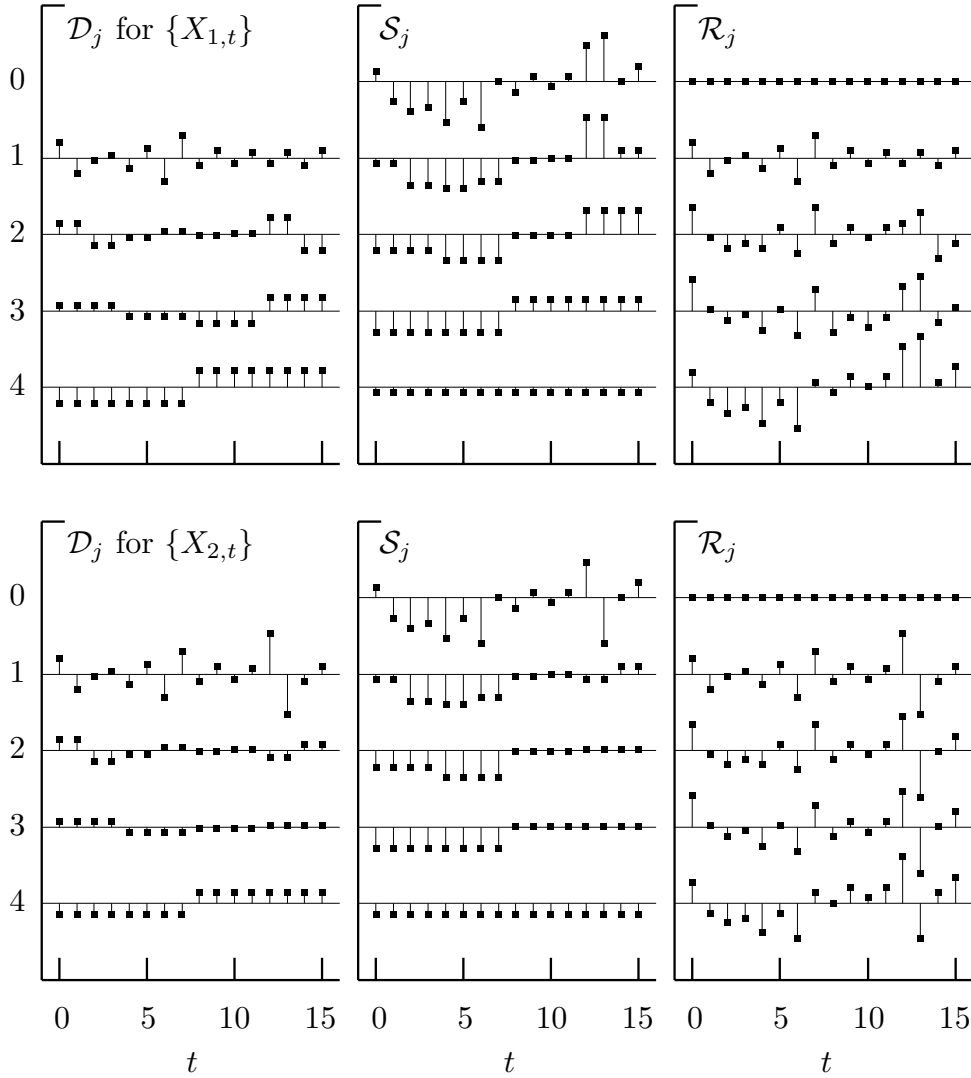
Figure 64. Haar wavelet details $\mathcal{D}_j$, smooths $\mathcal{S}_j$ and roughs $\mathcal{R}_j$ of levels $j = 0$ to 4 for $\{X_{1,t}\}$ (top plots) and $\{X_{2,t}\}$ (bottom). For any given j, we have $\mathcal{S}_j + \mathcal{R}_j = \mathbf{X}$. The jth detail can be interpreted as the difference between successive smooths or successive roughs: $\mathcal{D}_j = \mathcal{S}_{j-1} - \mathcal{S}_j$ and $\mathcal{D}_j = \mathcal{R}_j - \mathcal{R}_{j-1}$.
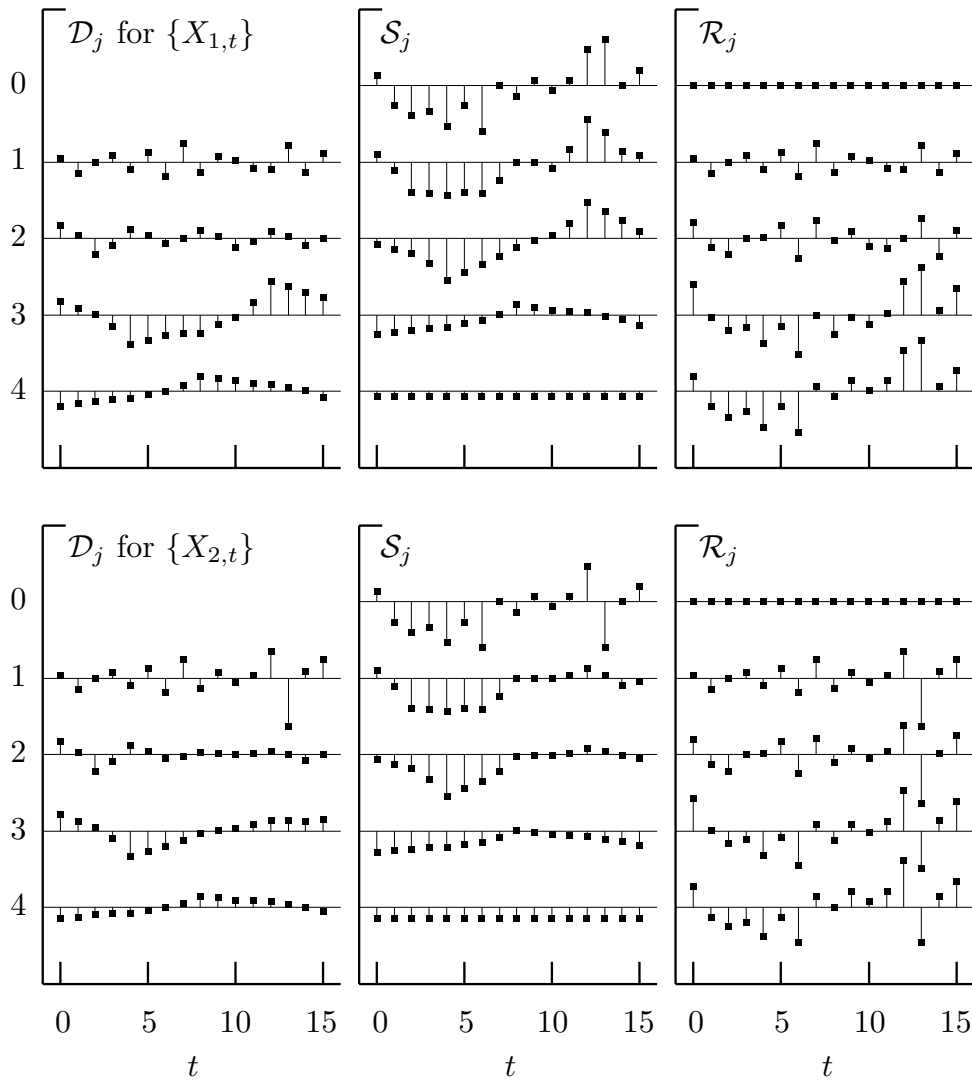
Figure 65. D(4) wavelet details $\mathcal{D}_j$, smooths $\mathcal{S}_j$ and roughs $\mathcal{R}_j$ for $\{X_{1,t}\}$ (top plots) and $\{X_{2,t}\}$ (bottom). Figure 64 has corresponding plots for the Haar wavelet. A comparison of these two figures shows that the Haar and D(4) smooths $\mathcal{S}_4$ agree perfectly for a given time series, which is a consequence of the fact that $\mathcal{V}_4$ is the same for both transforms (the roughs $\mathcal{R}_0$ also agree by definition).
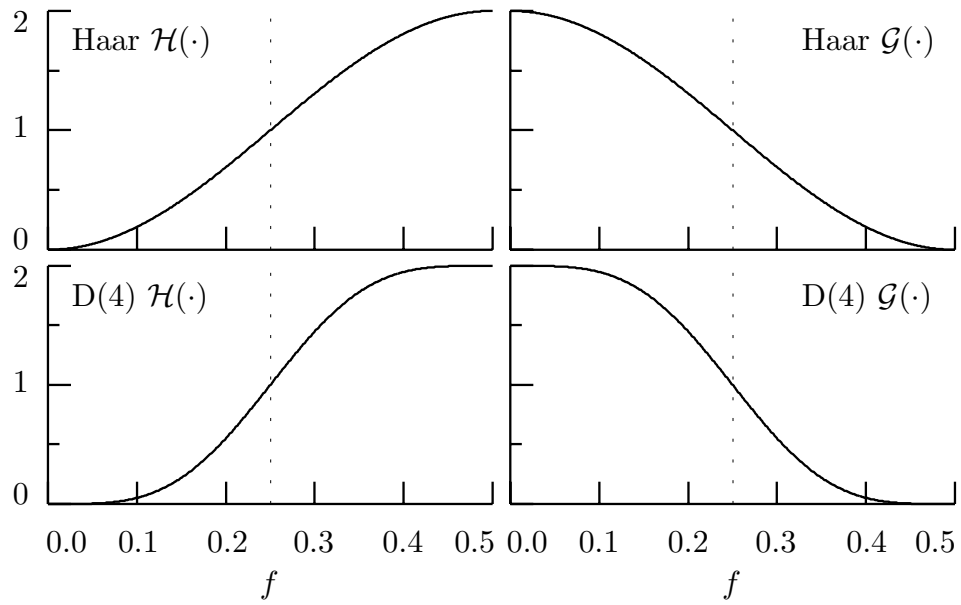
Figure 73. Squared gain functions for Haar wavelet filter (upper left-hand plot), Haar scaling filter (upper right), D(4) wavelet filter (lower left) and D(4) scaling filter (lower right). The dotted lines mark the frequency $f = 1/4$, which is the lower (upper) end of the nominal pass-band for the wavelet (scaling) filters.
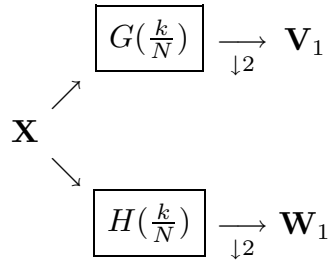
Figure 80. Flow diagram illustrating analysis of $\mathbf{X}$ into $\mathbf{W}_1$ and $\mathbf{V}_1$. The time series in the vector $\mathbf{X}$ of length N is circularly filtered using a wavelet filter $H(\cdot)$ periodized to length N (the frequency domain form of this filter is given by $\{H(\frac{k}{N}) : k = 0, \ldots, N - 1\}$). All the odd indexed values of the filtered series are used to form the vector $\mathbf{W}_1$ of length $N/2$ containing the wavelet coefficients of level $j = 1$ ('$\downarrow 2$' indicates downsampling by two); in a similar manner, the vector $\mathbf{V}_1$ of length $N/2$ containing the scaling coefficients of level $j = 1$ is obtained by downsampling the output from filtering $\mathbf{X}$ with the scaling filter $G(\cdot)$ periodized to length N.
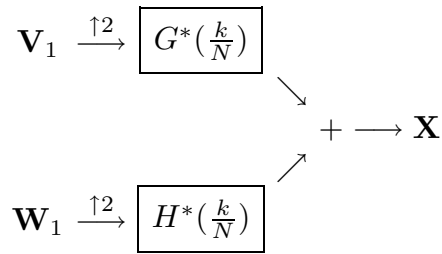
$$\mathbf{V}_1 \xrightarrow{\uparrow 2} \boxed{G^*(\tfrac{k}{N})}$$

$$+ \longrightarrow \mathbf{X}$$

$$\mathbf{W}_1 \xrightarrow{\uparrow 2} \boxed{H^*(\tfrac{k}{N})}$$

Figure 83. Flow diagram illustrating synthesis of $\mathbf{X}$ from $\mathbf{W}_1$ and $\mathbf{V}_1$. The vector $\mathbf{W}_1$ of length $N/2$ is upsampled by two to form a vector of length N, whose contents are then circularly filtered using the filter $\{H^*(\tfrac{k}{N})\}$ (here upsampling $\mathbf{W}_1$ by two means adding a zero before each element in that vector and is indicated on the flow diagram by '$\uparrow$ 2'). The vector $\mathbf{X}$ is formed by adding the output from this filter to a similar output obtained by filtering $\mathbf{V}_1$ (after upsampling) with the filter $\{G^*(\tfrac{k}{N})\}$.
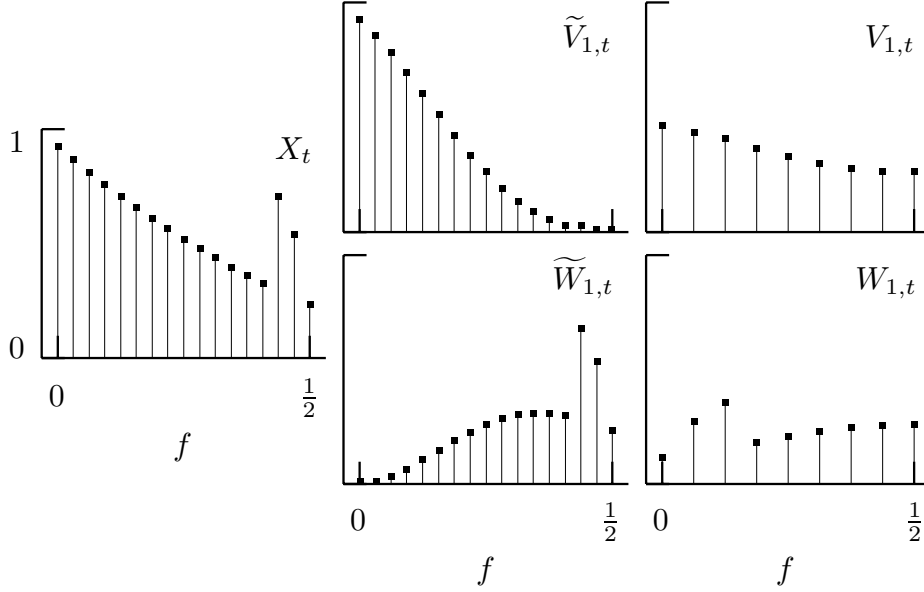
Figure 86. Magnitude squared DFT of the time series $\{X_t\}$ of Equation (85) (left-hand plot), along with the magnitude squared DFTs for the rescaled Haar scaling and wavelet filter outputs $\{\widetilde{V}_{1,t}\}$ and $\{\widetilde{W}_{1,t}\}$ (middle plots) and the Haar scaling and wavelet coefficients $\{V_{1,t}\}$ and $\{W_{1,t}\}$ (right-hand). Because $\{X_t\}$ and its filtered versions are real-valued, the squared magnitudes of all the DFTs are symmetric about zero, so just the values for the nonnegative Fourier frequencies are shown. The magnitude squared DFTs for $\{\widetilde{V}_{1,t}\}$ and $\{\widetilde{W}_{1,t}\}$ are obtained by multiplying the magnitude squared DFT for $\{X_t\}$ by values picked from the squared gain functions for $\{g_l/\sqrt{2}\}$ and $\{h_l/\sqrt{2}\}$ (these are defined by $\mathcal{G}(f)/2$ and $\mathcal{H}(f)/2$ – the shapes of these functions are shown in the top row of Figure 73). Note that $\{\widetilde{V}_{1,t}\}$ preserves the low frequency content of $\{X_t\}$ in its low frequencies, while $\{\widetilde{W}_{1,t}\}$ preserves the high frequency content of $\{X_t\}$ in its high frequencies. Whereas $\{\widetilde{V}_{1,t}\}$ and $\{\widetilde{W}_{1,t}\}$ are deficient in, respectively, high and low frequency content and hence are half-band series, the subsampled and rescaled series $\{V_{1,t}\}$ and $\{W_{1,t}\}$ are full-band series that preserve, respectively, the low and high frequency content of $\{X_t\}$. Whereas $\{V_{1,t}\}$ keeps the ordering of the frequencies in $\{X_t\}$, the ordering is reversed in $\{W_{1,t}\}$; e.g., the bulge at the high frequencies $f_{14} = \frac{14}{32}$ and $f_{15} = \frac{15}{32}$ in the DFT for $\{X_t\}$ appears in a reversed manner at the low frequencies $f'_1 = \frac{1}{16}$ and $f'_2 = \frac{2}{16}$ in the DFT for $\{W_{1,t}\}$.
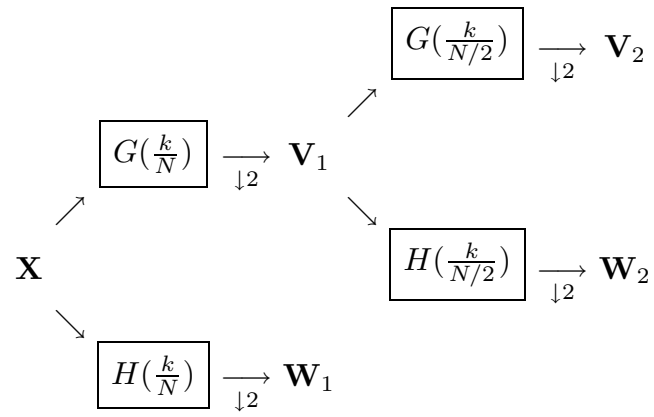
$$
\begin{array}{c}
\boxed{G(\tfrac{k}{N/2})} \xrightarrow[\downarrow 2]{} \mathbf{V}_2 \\[2em]
\boxed{G(\tfrac{k}{N})} \xrightarrow[\downarrow 2]{} \mathbf{V}_1 \\[2em]
\mathbf{X} \qquad \boxed{H(\tfrac{k}{N/2})} \xrightarrow[\downarrow 2]{} \mathbf{W}_2 \\[2em]
\boxed{H(\tfrac{k}{N})} \xrightarrow[\downarrow 2]{} \mathbf{W}_1
\end{array}
$$

Figure 89. Flow diagram illustrating analysis of $\mathbf{X}$ into $\mathbf{W}_1$, $\mathbf{W}_2$ and $\mathbf{V}_2$.

$$\mathbf{V}_2 \xrightarrow{\uparrow 2} \boxed{G^*(\tfrac{k}{N/2})}$$

$$\mathbf{W}_2 \xrightarrow{\uparrow 2} \boxed{H^*(\tfrac{k}{N/2})}$$

$$+ \longrightarrow \mathbf{V}_1 \xrightarrow{\uparrow 2} \boxed{G^*(\tfrac{k}{N})}$$

$$+ \longrightarrow \mathbf{X}$$

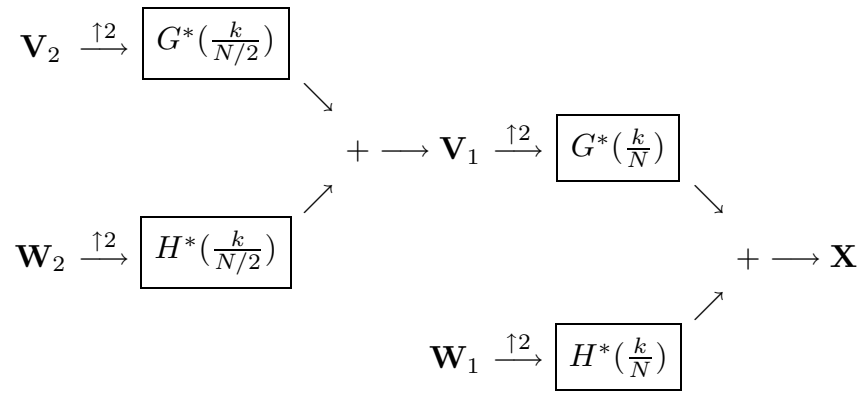$$\mathbf{W}_1 \xrightarrow{\uparrow 2} \boxed{H^*(\tfrac{k}{N})}$$

Figure 90. Flow diagram illustrating synthesis of $\mathbf{X}$ from $\mathbf{W}_1$, $\mathbf{W}_2$ and $\mathbf{V}_2$.
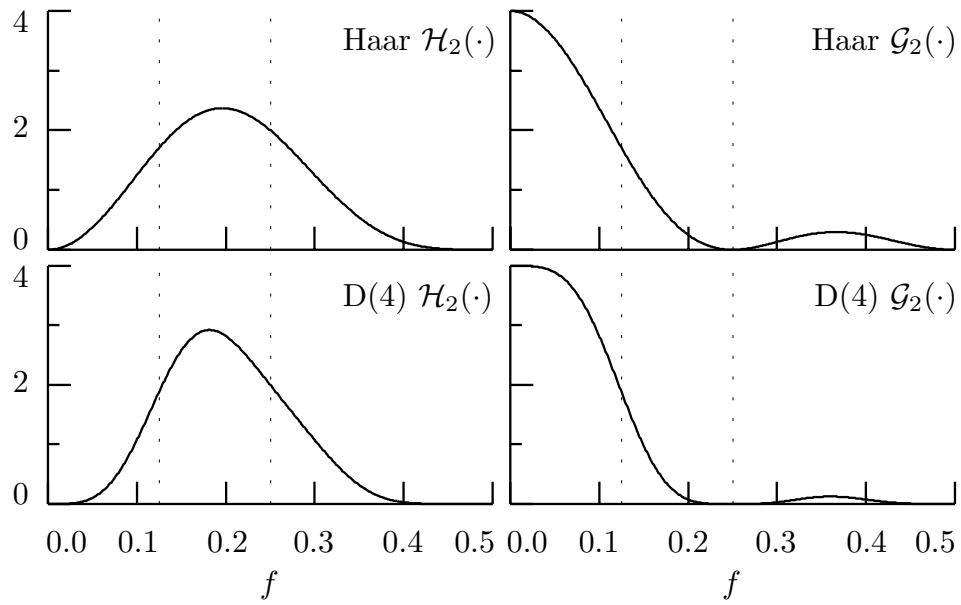
Figure 91. Squared gain functions for Haar $\{h_{2,l}\}$ and $\{g_{2,l}\}$ filters (upper left and right-hand plots, respectively) and D(4) $\{h_{2,l}\}$ and $\{g_{2,l}\}$ filters (lower left and right). The dotted lines mark the frequencies $f = 1/8$ and $f = 1/4$.
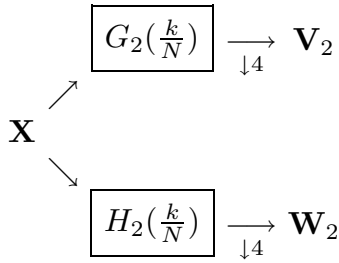
Figure 92. Flow diagram illustrating generation of $\mathbf{W}_2$ and $\mathbf{V}_2$ from $\mathbf{X}$. The time series in the vector $\mathbf{X}$ of length N is circularly filtered using the length N periodized version of the $j = 2$ level wavelet filter $\{h_{2,l}\}$ with transfer function $H_2(\cdot)$. All values of the filtered series with indices t such that $t + 1 \bmod 4 = 0$ are used to form the vector $\mathbf{W}_2$ ('$\downarrow 4$' indicates downsampling every fourth value). The $N/4$ elements of $\mathbf{W}_2$ are the wavelet coefficients of level $j = 2$. Likewise, the vector $\mathbf{V}_2$ of length $N/4$ contains the scaling coefficients of level $j = 2$ and is obtained by downsampling (by four) the output from filtering $\mathbf{X}$ with the circular filter whose frequency domain representation is $\{G_2(\frac{k}{N})\}$.
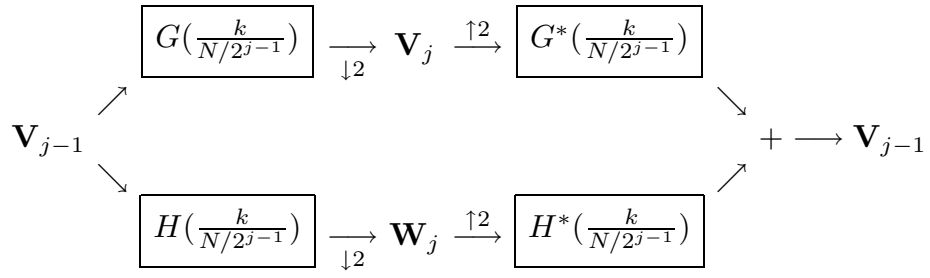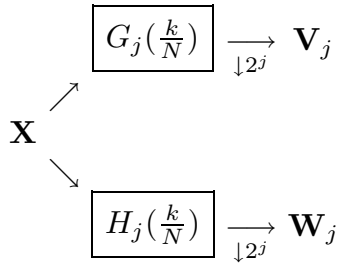
$$\mathbf{V}_{j-1} \nearrow \boxed{G\!\left(\frac{k}{N/2^{j-1}}\right)} \xrightarrow[\downarrow 2]{} \mathbf{V}_j \xrightarrow{\uparrow 2} \boxed{G^*\!\left(\frac{k}{N/2^{j-1}}\right)} \searrow$$

$$\mathbf{V}_{j-1} \searrow \boxed{H\!\left(\frac{k}{N/2^{j-1}}\right)} \xrightarrow[\downarrow 2]{} \mathbf{W}_j \xrightarrow{\uparrow 2} \boxed{H^*\!\left(\frac{k}{N/2^{j-1}}\right)} \nearrow \quad + \longrightarrow \mathbf{V}_{j-1}$$

Figure 94. Flow diagram illustrating analysis of $\mathbf{V}_{j-1}$ into $\mathbf{W}_j$ and $\mathbf{V}_j$, followed by synthesis of $\mathbf{V}_{j-1}$ from $\mathbf{W}_j$ and $\mathbf{V}_j$.

Figure 96. Flow diagram illustrating generation of $\mathbf{W}_j$ and $\mathbf{V}_j$ from $\mathbf{X}$. The time series in the vector $\mathbf{X}$ of length N is circularly filtered using a jth level wavelet filter $\{h_{j,l}\}$ with transfer function $H_j(\cdot)$, and all values of the filtered series with indices divisible by 2^j are used to form the vector $\mathbf{W}_j$ of length $N/2^j$ containing the wavelet coefficients of level j ('$\downarrow 2^j$' indicates downsampling every 2^jth value); in a similar manner, the vector $\mathbf{V}_j$ of length $N/2^j$ containing the scaling coefficients of level j is obtained by downsampling the output from filtering $\mathbf{X}$ using the jth level scaling filter with transfer function $G_j(\cdot)$.
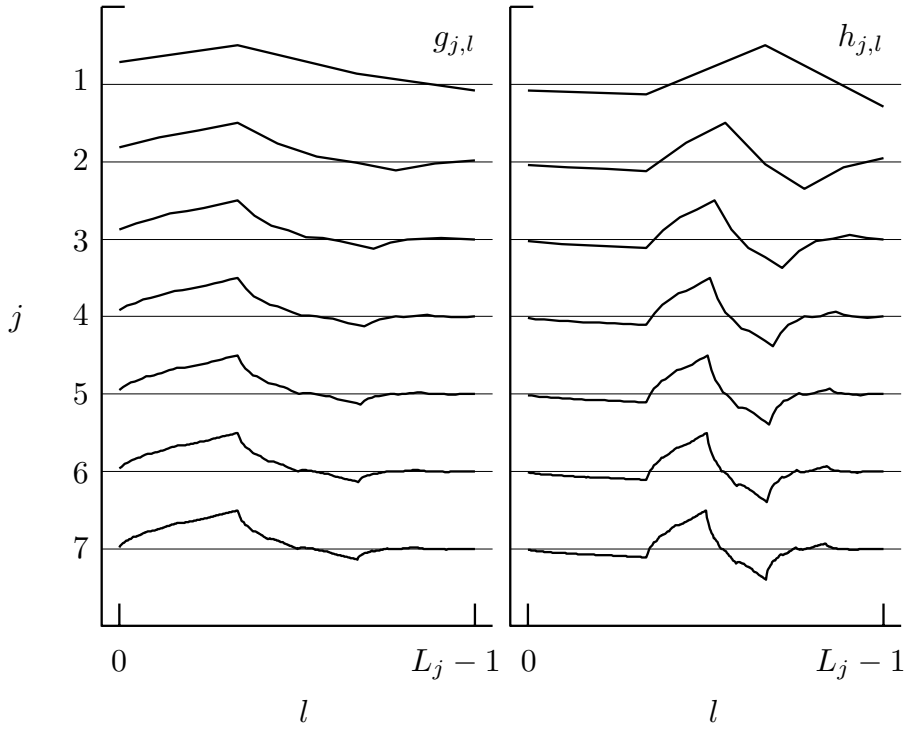
Figure 98a. D(4) scaling $\{g_{j,l}\}$ and wavelet $\{h_{j,l}\}$ filters for scales indexed by $j = 1, 2, \ldots, 7$ (here the individual values of the impulse response sequences are connected by lines).
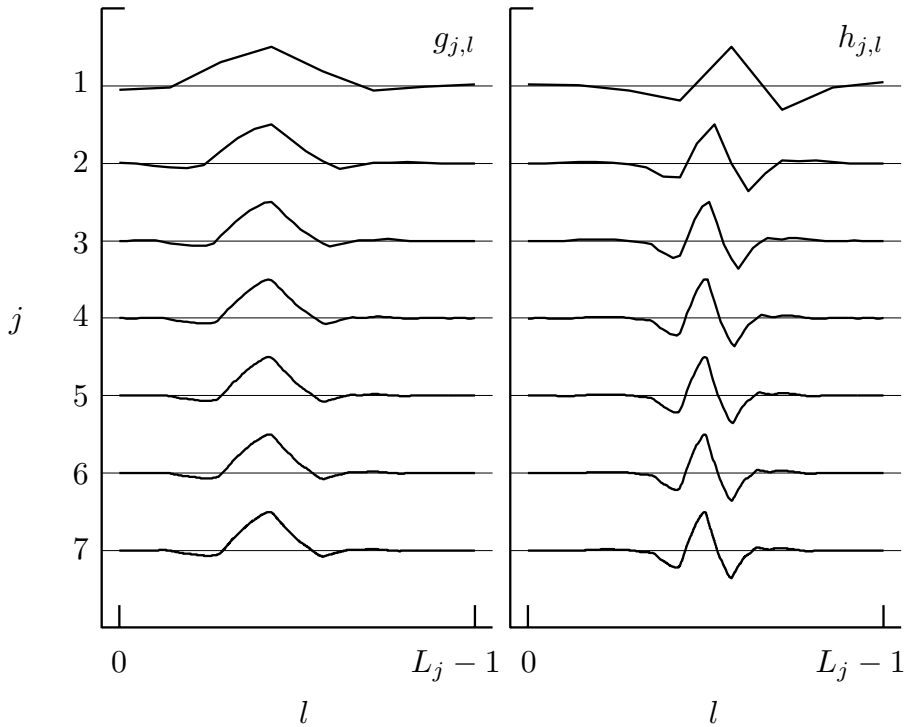

Figure 98b. LA(8) scaling $\{g_{j,l}\}$ and wavelet $\{h_{j,l}\}$ filters for scales indexed by $j = 1, 2, \ldots, 7$ (here the individual values of the impulse response sequences are connected by lines). These filters are defined in Section 4.8.
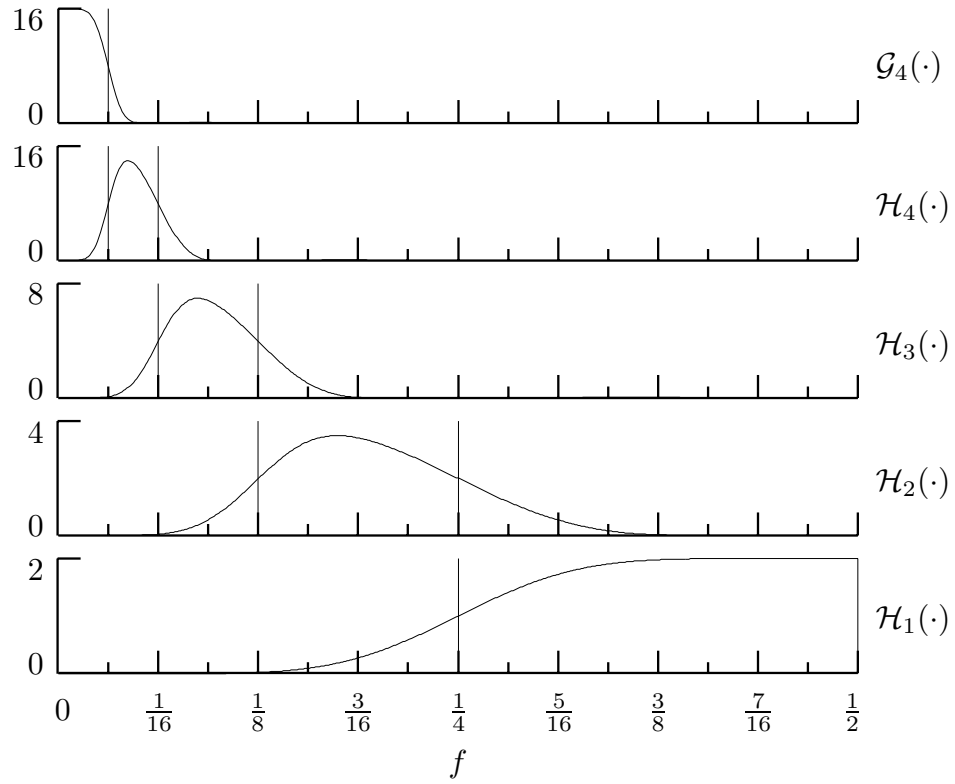
Figure 99. Squared gain functions for LA(8) filters $\{h_{j,l}\}, j = 1, \ldots, 4$, and $\{g_{4,l}\}$ (these filters are defined in Section 4.8).
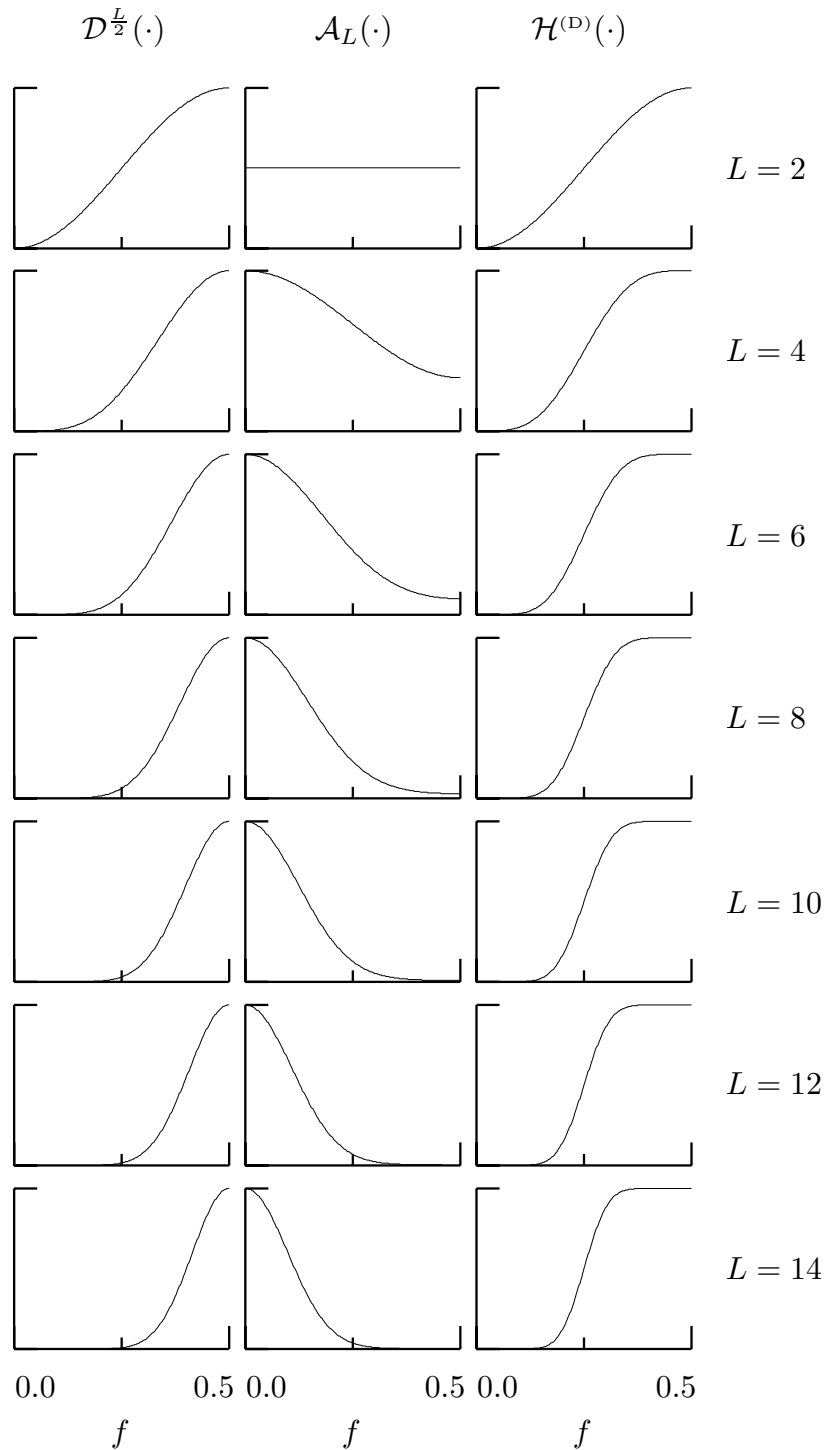
Figure 107. Squared gain functions $\mathcal{H}^{(\mathrm{D})}(\cdot)$ for Daubechies wavelet filters of widths $L = 2, 4, \ldots, 14$ (right-hand column). Each $\mathcal{H}^{(\mathrm{D})}(\cdot)$ is the product of two other squared gain functions, namely, $\mathcal{D}^{\frac{L}{2}}(\cdot)$ (left-hand column) and $\mathcal{A}_L(\cdot)$ (middle). The first corresponds to an $\frac{L}{2}$ order difference filter, while for $L \geq 4$ the second is associated with a weighted average (i.e., low-pass filter).
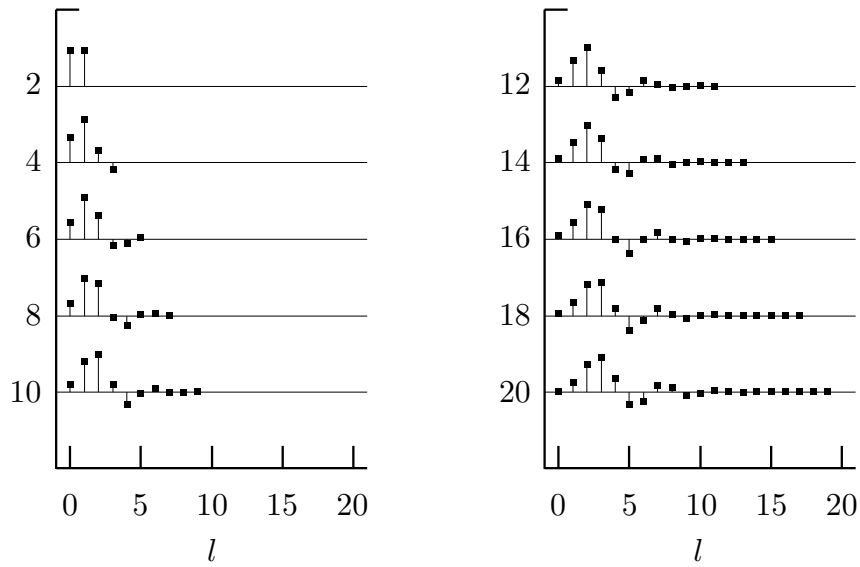
Figure 108a. Daubechies extremal phase scaling filters $\{g_l^{(\mathrm{ep})}\}$ for $L = 2, 4, \ldots, 20$ (values based on Daubechies, 1992, p. 195, Table 6.1).
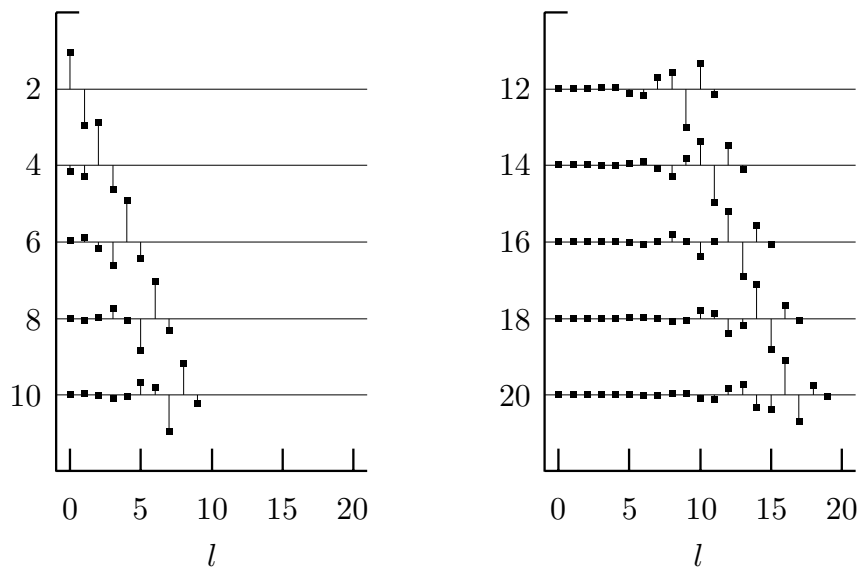

Figure 108b. Daubechies wavelet filters corresponding to the extremal phase scaling filters in Figure 108a.

l	g_l for D(6)	g_l for C(6)	g_l for D(8)
0	0.3326705529500827	−0.0156557285289848	0.2303778133074431
1	0.8068915093110928	−0.0727326213410511	0.7148465705484058
2	0.4598775021184915	0.3848648565381134	0.6308807679358788
3	−0.1350110200102546	0.8525720416423900	−0.0279837694166834
4	−0.0854412738820267	0.3378976709511590	−0.1870348117179132
5	0.0352262918857096	−0.0727322757411889	0.0308413818353661
6			0.0328830116666778
7			−0.0105974017850021

l	g_l for LA(8)	g_l for LA(12)	g_l for LA(16)
0	−0.0757657147893407	0.0154041093273377	−0.0033824159513594
1	−0.0296355276459541	0.0034907120843304	−0.0005421323316355
2	0.4976186676324578	−0.1179901111484105	0.0316950878103452
3	0.8037387518052163	−0.0483117425859981	0.0076074873252848
4	0.2978577956055422	0.4910559419276396	−0.1432942383510542
5	−0.0992195435769354	0.7876411410287941	−0.0612733590679088
6	−0.0126039672622612	0.3379294217282401	0.4813596512592012
7	0.0322231006040713	−0.0726375227866000	0.7771857516997478
8		−0.0210602925126954	0.3644418948359564
9		0.0447249017707482	−0.0519458381078751
10		0.0017677118643983	−0.0272190299168137
11		−0.007800708324765	0.0491371796734768
12			0.0038087520140601
13			−0.0149522583367926
14			−0.0003029205145516
15			0.0018899503329007

Table 109. Coefficients for selected Daubechies scaling filters and for the coiflet scaling filter for $L = 6$ (the latter is discussed in Section 4.9). The coefficients in this table are derived from Daubechies (1992, 1993). These coefficients (and those for other $\{g_l\}$) are available on the Web site for this book (see page *xiv*).
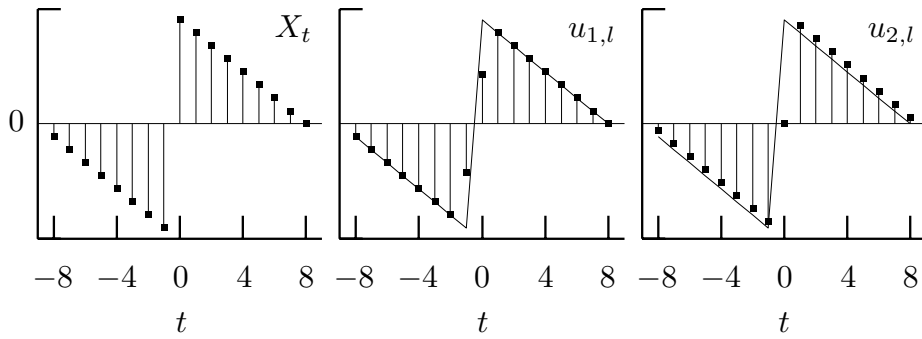
Figure 110. Example of filtering using a zero phase filter. The left-hand plot shows a time series $\{X_t\}$ with a discontinuity from $t = -1$ to $t = 0$. The solid points in the middle and right-hand plots show the results of filtering this series with, respectively, the filters $\{u_{1,l}\}$ (Equation (110a)) and $\{u_{2,l}\}$ (Equation (110b)), only the first of which has zero phase. The thin curves on these two plots show the original time series. Note that the discontinuity is spread out – but not shifted in location – using the zero phase filter $\{u_{1,l}\}$, whereas it is spread out and shifted forward in time using $\{u_{2,l}\}$.
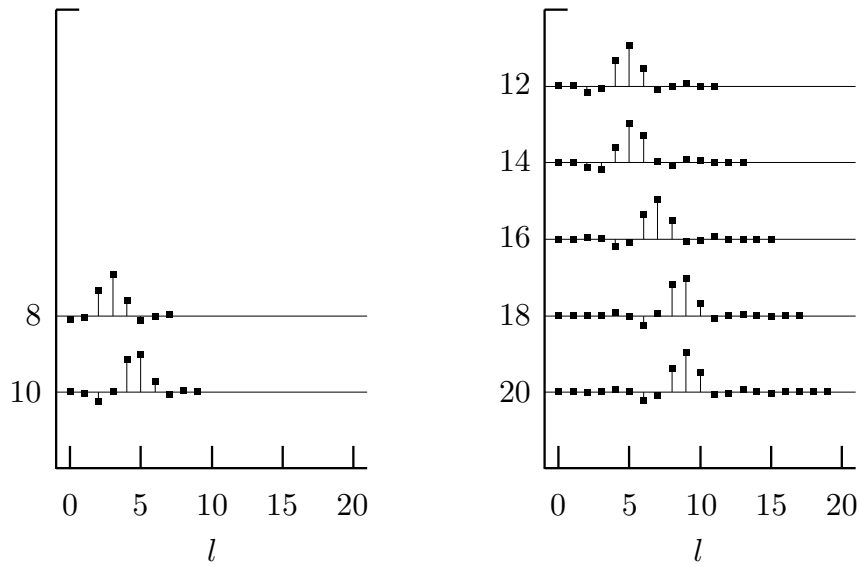
Figure 113a. Daubechies least asymmetric scaling filters $\{g_l^{(\mathrm{la})}\}$ for $L = 8, 10, \ldots, 20$ (values based on Daubechies, 1992, p. 198, Table 6.3, with modifications as noted in item [1] of the Comments and Extensions to this section).
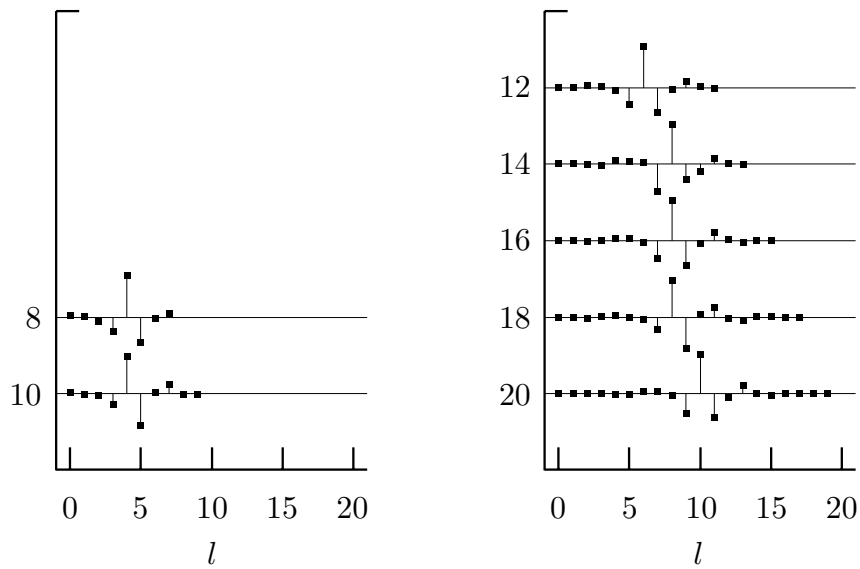

Figure 113b. Daubechies wavelet filters corresponding to the least asymmetric scaling filters shown in Figure 113a.
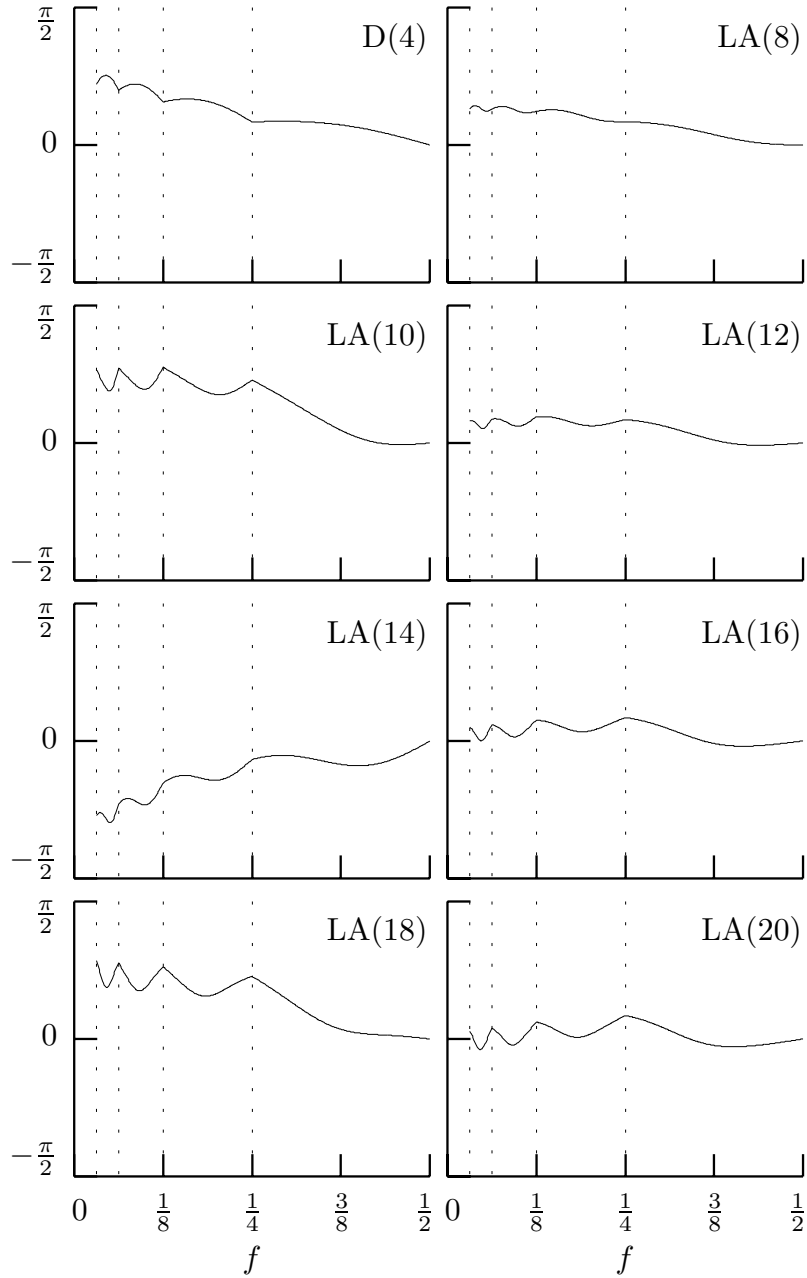
Figure 115. Exact phase functions of shifted LA wavelet filters $\{h_{j,l}\}$, $j = 1$, 2, 3 and 4 (the D(4) case is also shown, with shifts governed by setting $\nu = -1$). The phase functions for $\{h_{j,l}\}$ are plotted just over frequencies in the interval $[1/2^{j+1}, 1/2^j]$ – these intervals are indicated by the vertical dotted lines.

L	$|\nu| - e\{g_l\}$	L	$|\nu| - e\{g_l\}$
8	0.1536	14	-0.1615
10	0.4500	16	0.1546
12	0.1543	18	0.4471
		20	0.1547

Table 118. Comparison between advances $|p_j^{(H)}|$ and $|\nu_j^{(H)}|$ for Daubechies least asymmetric wavelet filters. Since $|p_j^{(H)}| - |\nu_j^{(H)}| = |\nu| - e\{g_l\}$ for all scale indices j, the above indicates that the two advances are the same when rounded to the nearest integer. To compare the advances for the corresponding scaling filters, the tabulated values must be multiplied by $2^j - 1$, so the advances diverge as j increases.
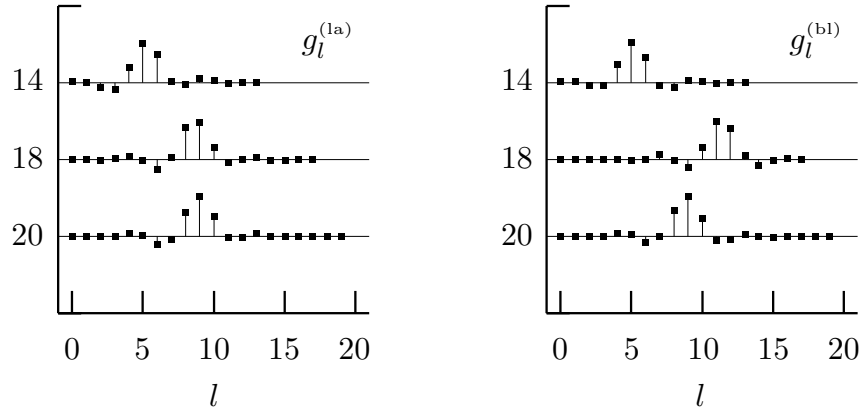
Figure 119. Least asymmetric scaling filters $\{g_l^{(\mathrm{la})}\}$ (left-hand column) and best localized scaling filters $\{g_l^{(\mathrm{bl})}\}$ (right) for $L = 14$, 18 and 20.
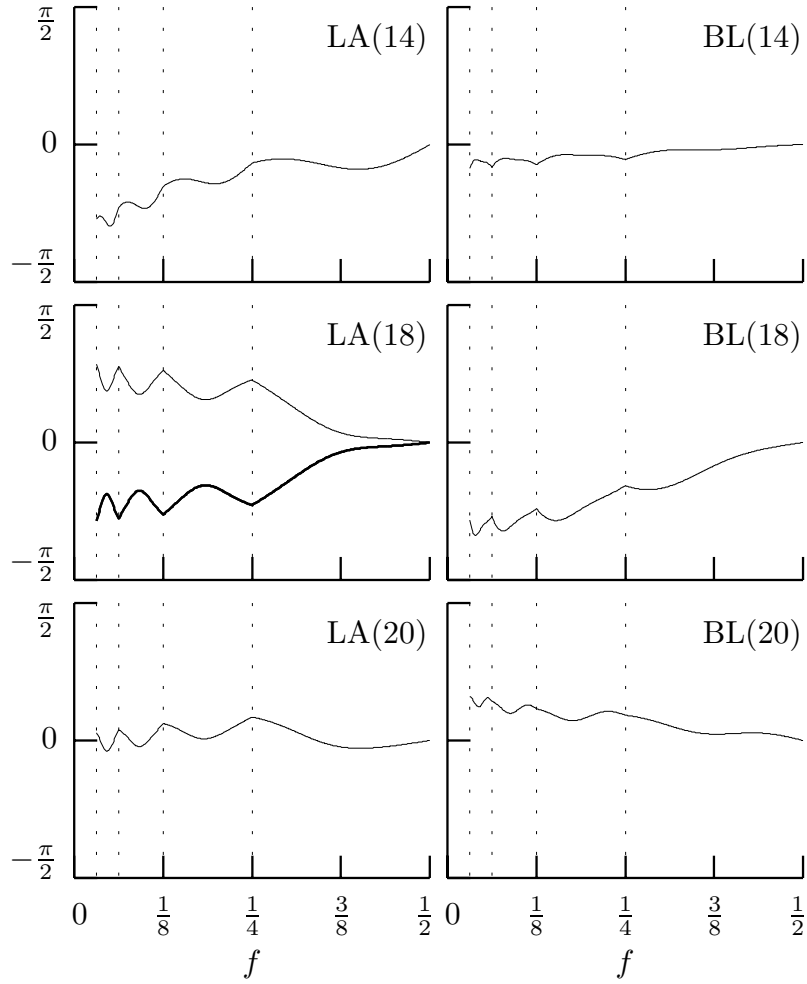
Figure 120. Exact phase functions of shifted least asymmetric and best localized wavelet filters (see the caption to Figure 115 and the text for details).
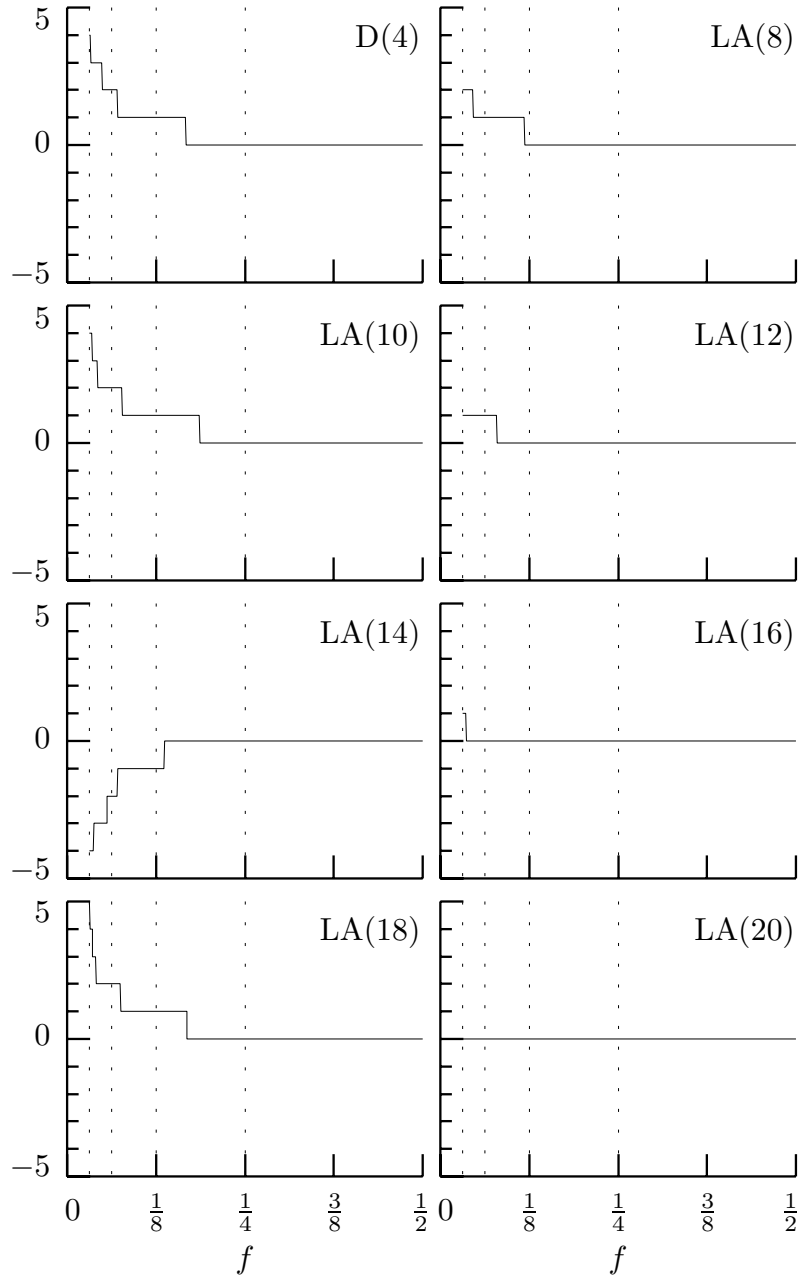
Figure 121. Time shift functions (rounded to the nearest integer) corresponding to the phase functions shown in Figure 115.
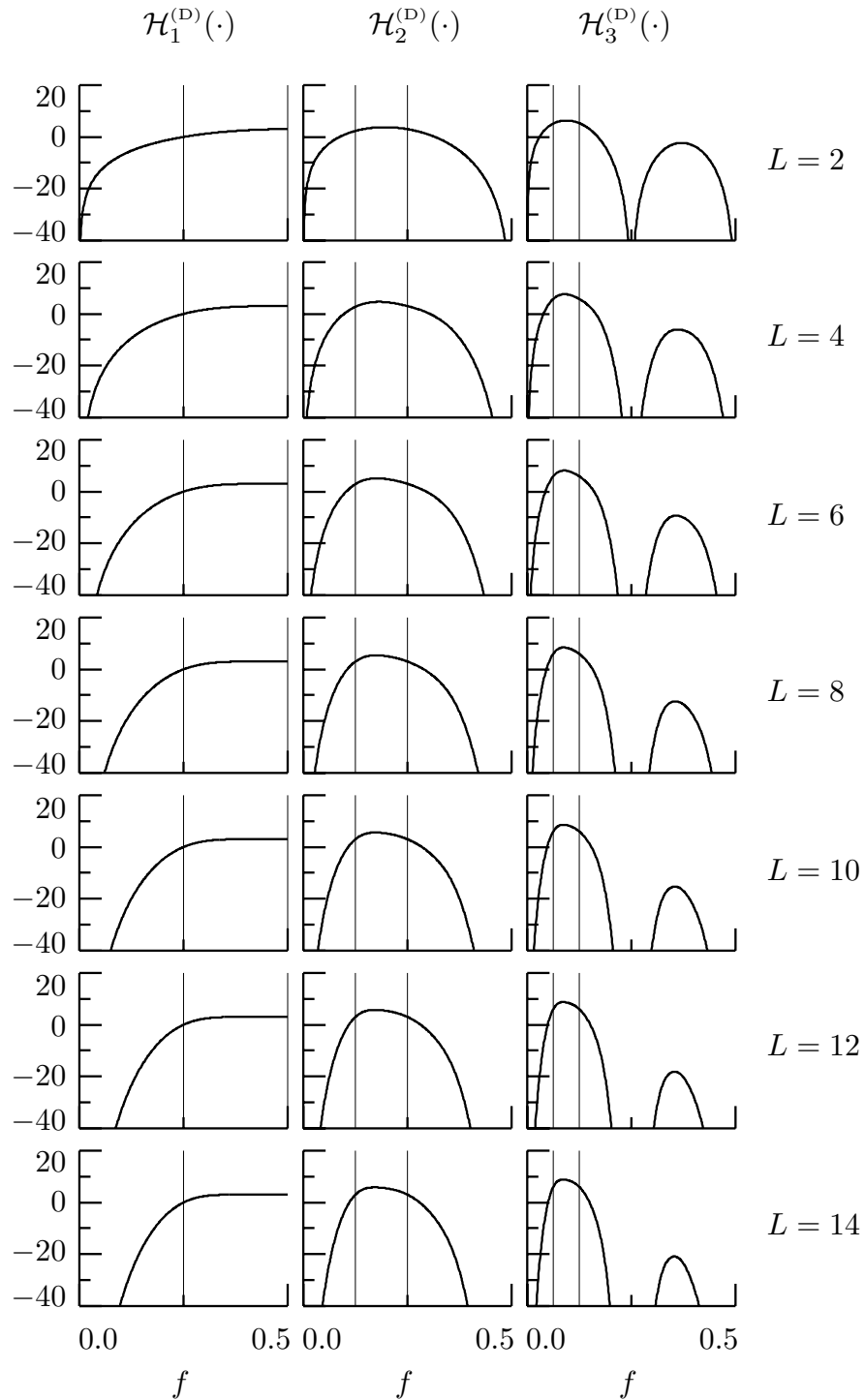
Figure 122. Squared gain functions $\mathcal{H}_j^{(\mathrm{D})}(\cdot)$, $j = 1, 2$ and 3 (left, middle and right columns, respectively), for Daubechies wavelet filters of widths $L = 2, 4, \ldots, 14$ (top to bottom rows, respectively). The two thin vertical lines in each plot delineate the nominal pass-band for the filter. The vertical axis is in decibels (i.e., we plot $10 \cdot \log_{10}(\mathcal{H}_j^{(\mathrm{D})}(f))$ versus f).
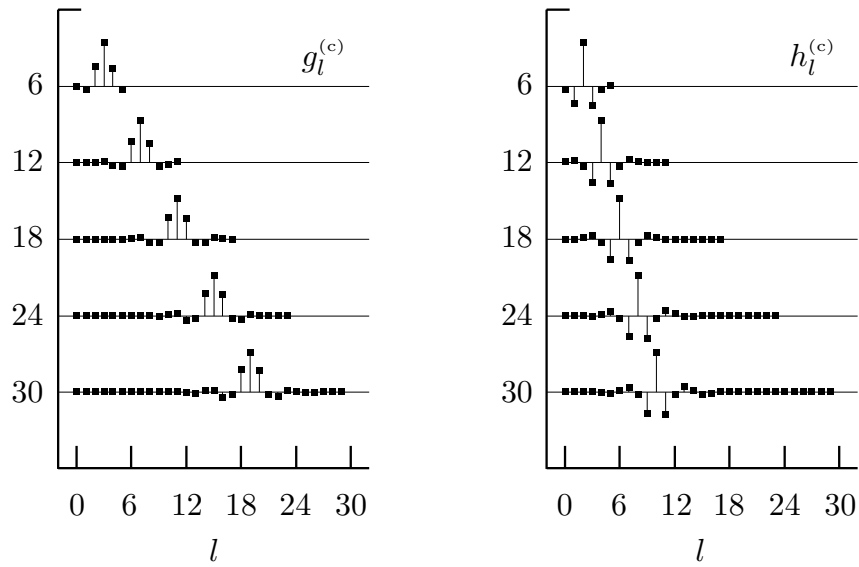
Figure 123. Coiflet scaling filters $\{g_l^{(c)}\}$ (left-hand column) and corresponding wavelet filters $\{h_l^{(c)}\}$ (right) of widths $L = 6, 12, 18, 24$ and 30 (Daubechies, 1992, p. 261, Table 8.1).
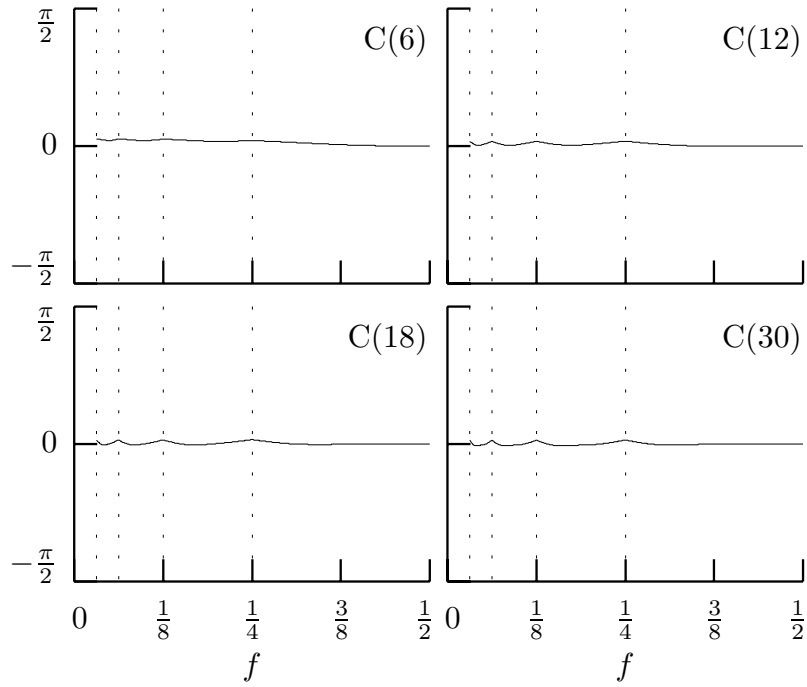
Figure 124. Exact phase functions of shifted coiflet wavelet filters (see the caption to Figure 115 and the text for details).
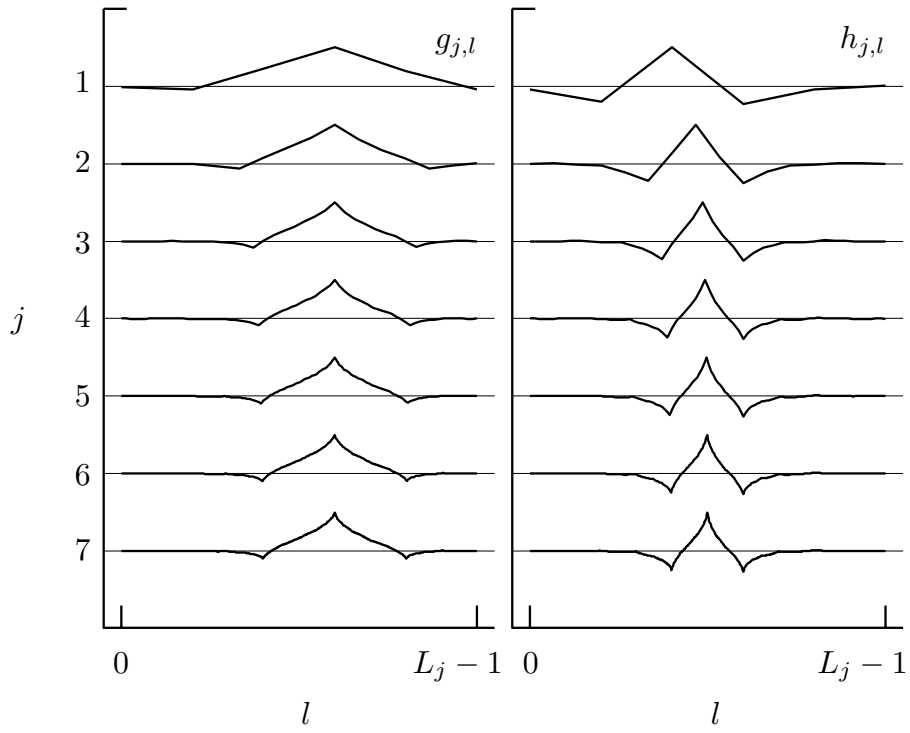
Figure 125. C(6) scaling $\{g_{j,l}\}$ and wavelet $\{h_{j,l}\}$ filters for scales indexed by $j = 1, 2, \ldots, 7$ (see Figures 98a and 98b for similar plots of the D(4) and LA(8) filters).
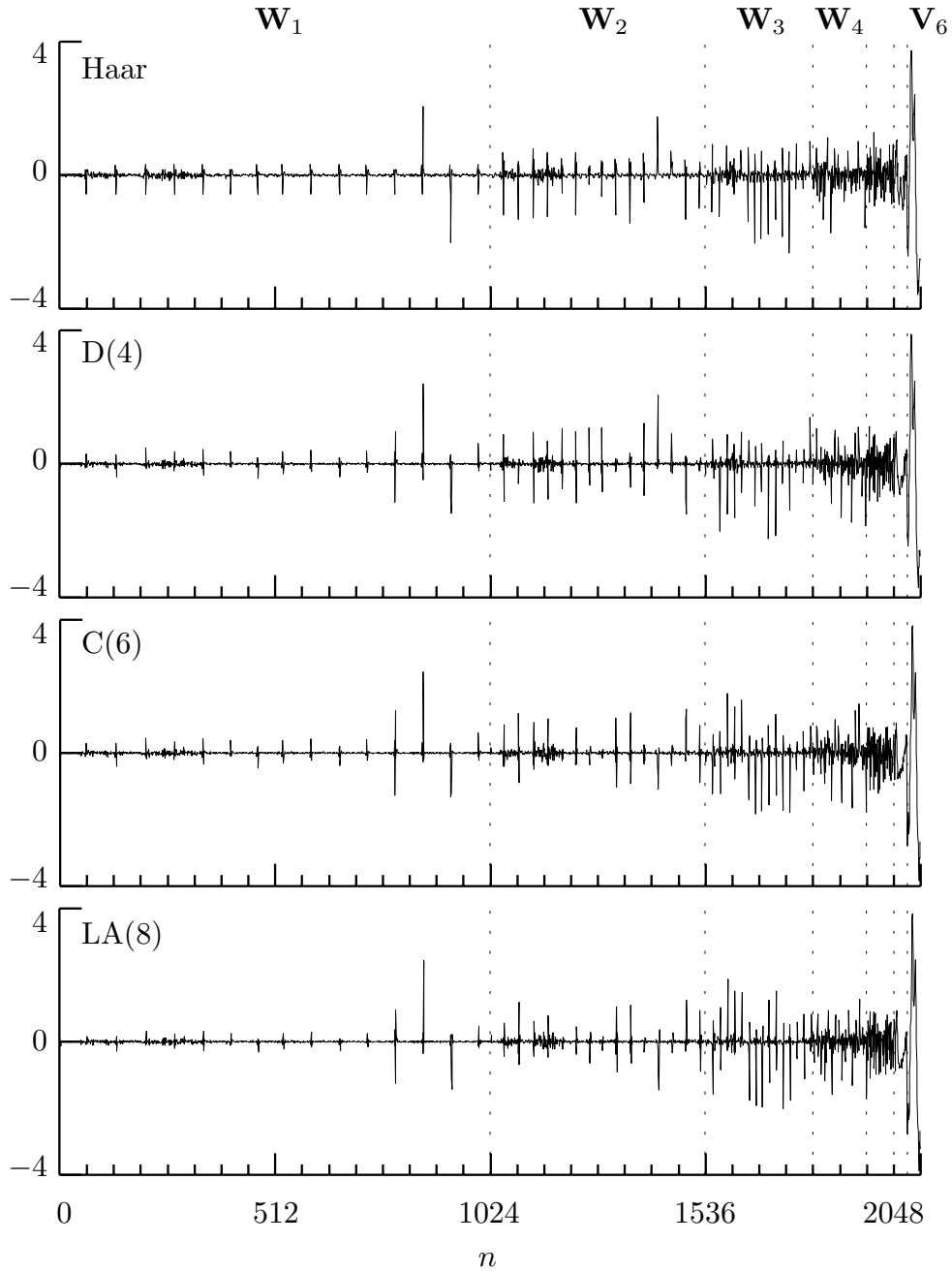
Figure 126. Partial DWT coefficients $\mathbf{W}$ of level $J_0 = 6$ for ECG time series using the Haar, D(4), C(6) and LA(8) wavelets. The elements W_n of $\mathbf{W}$ are plotted versus $n = 0, \dots, N-1 = 2047$. The six vertical dotted lines delineate the seven subvectors of $\mathbf{W}$, namely, $\mathbf{W}_1, \dots, \mathbf{W}_6$ and $\mathbf{V}_6$ ($\mathbf{W}_5$ and $\mathbf{W}_6$ are not labeled at the top of the figure due to lack of space).
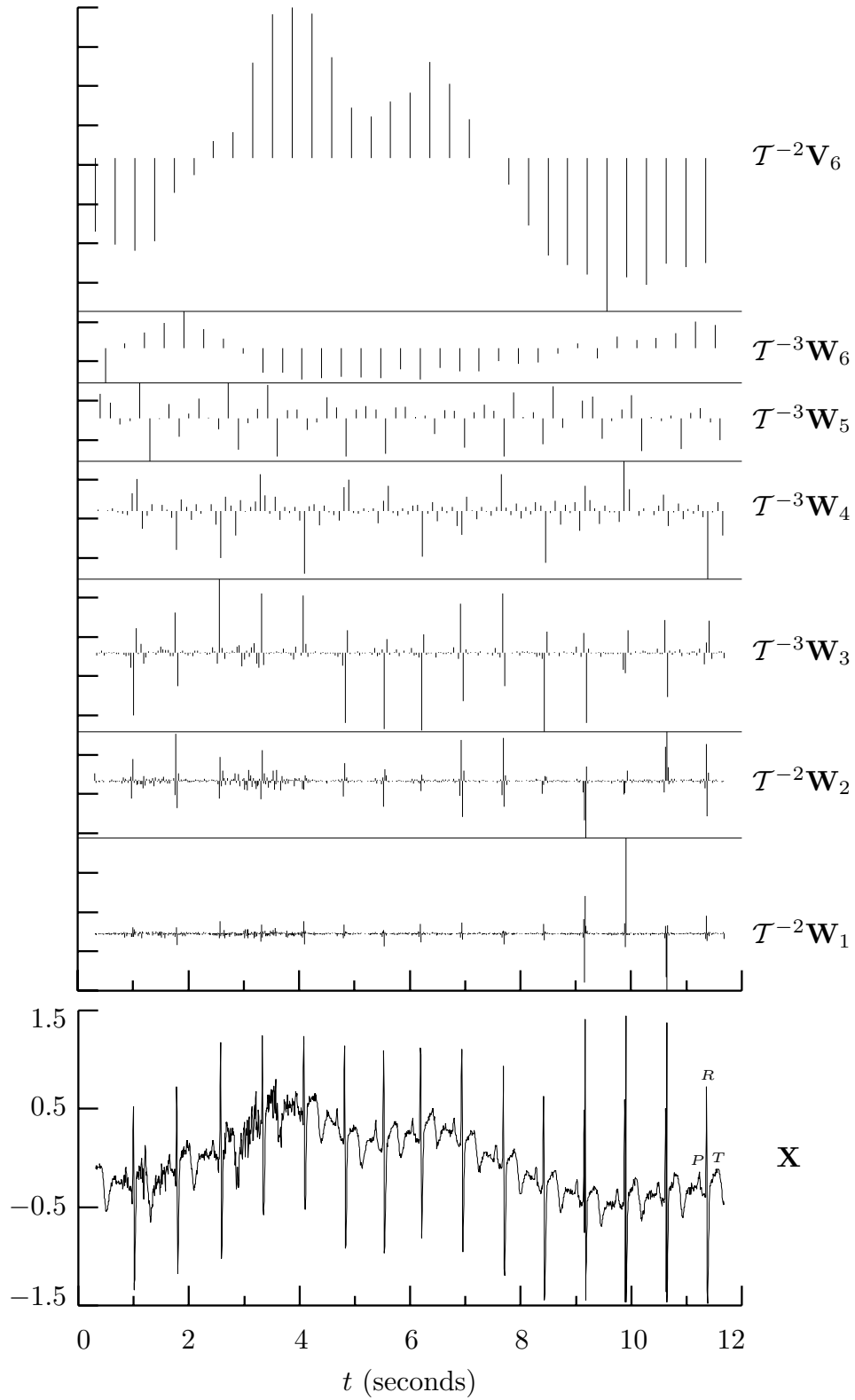
Figure 127. LA(8) DWT coefficients for ECG time series (data courtesy of Gust Bardy and Per Reinhall, University of Washington).
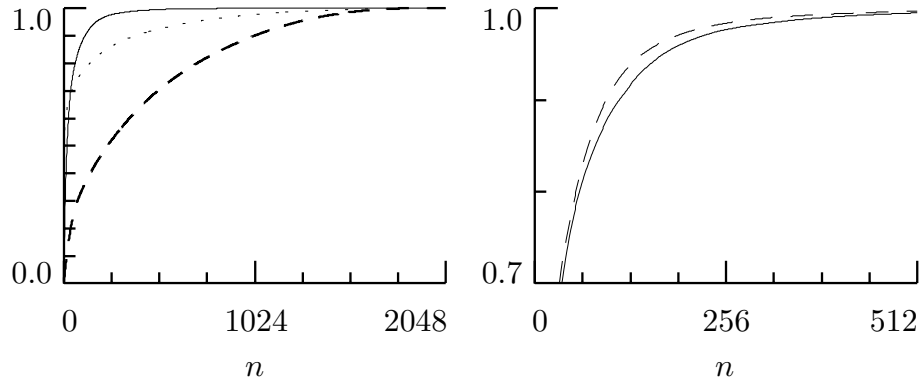
Figure 128. Normalized partial energy sequences. The left-hand plot has the NPESs for the original time series (thick dashed curve), the ODFT (dotted) and the Haar DWT (solid). The right-hand plot shows portions of the NPESs for the Haar DWT (solid curve again) and the D(4) DWT (thin dashed). The NPESs for the C(6) and LA(8) DWTs are virtually identical to the D(4) NPES.
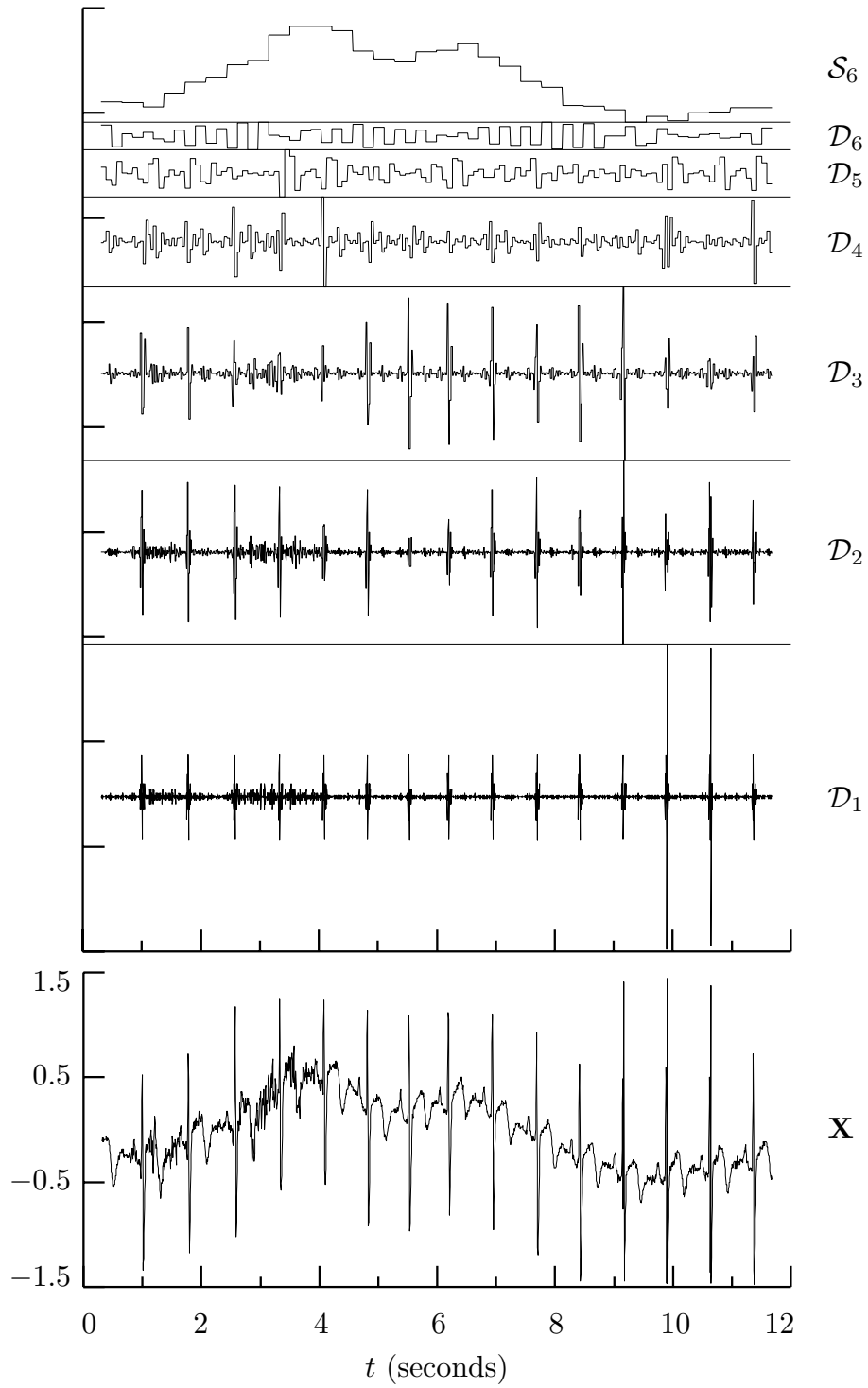
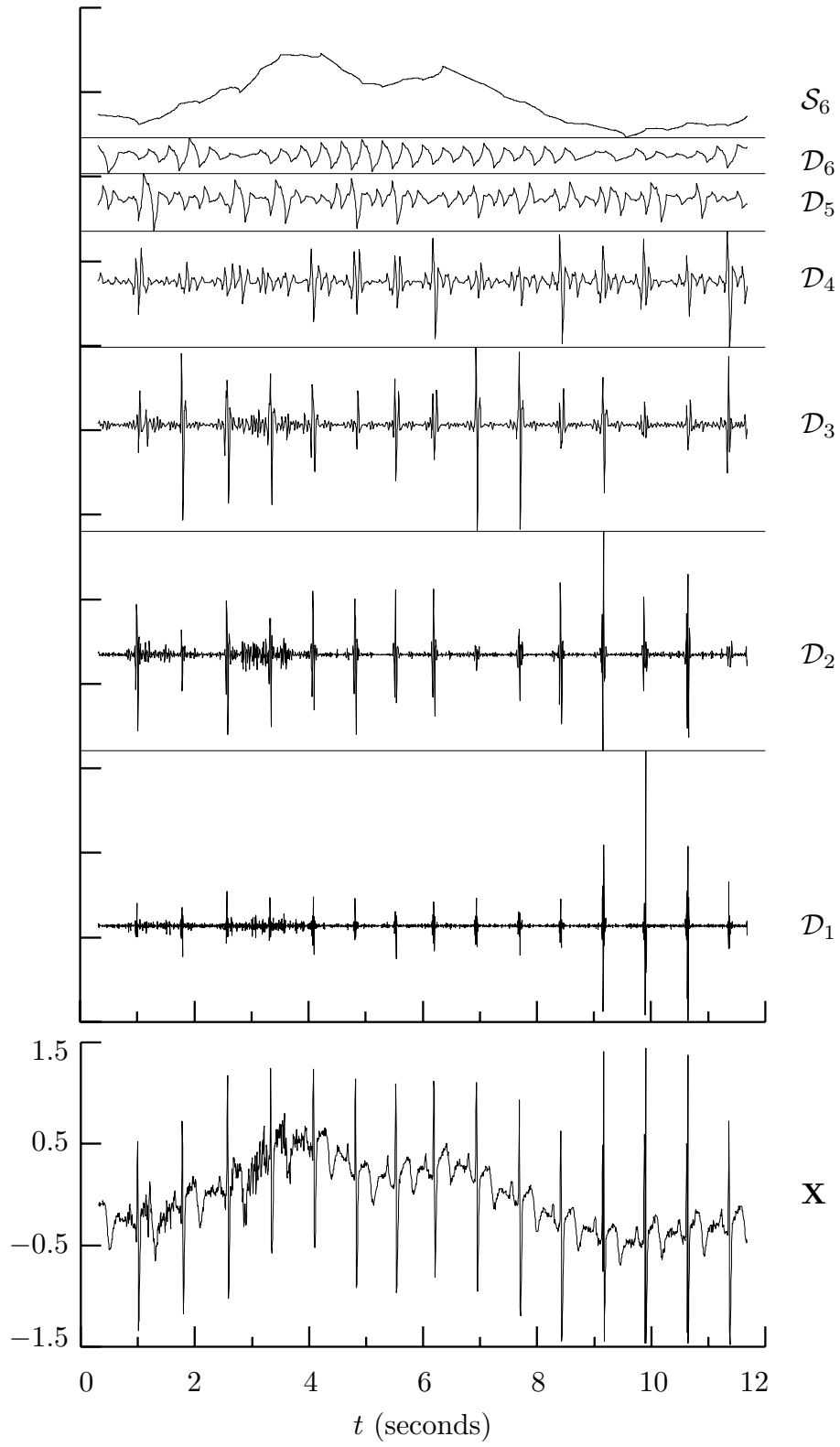**Figure 130.** Haar DWT multiresolution analysis of ECG time series (see text for details).

Figure 131. D(4) DWT multiresolution analysis of ECG time series (see text for details).
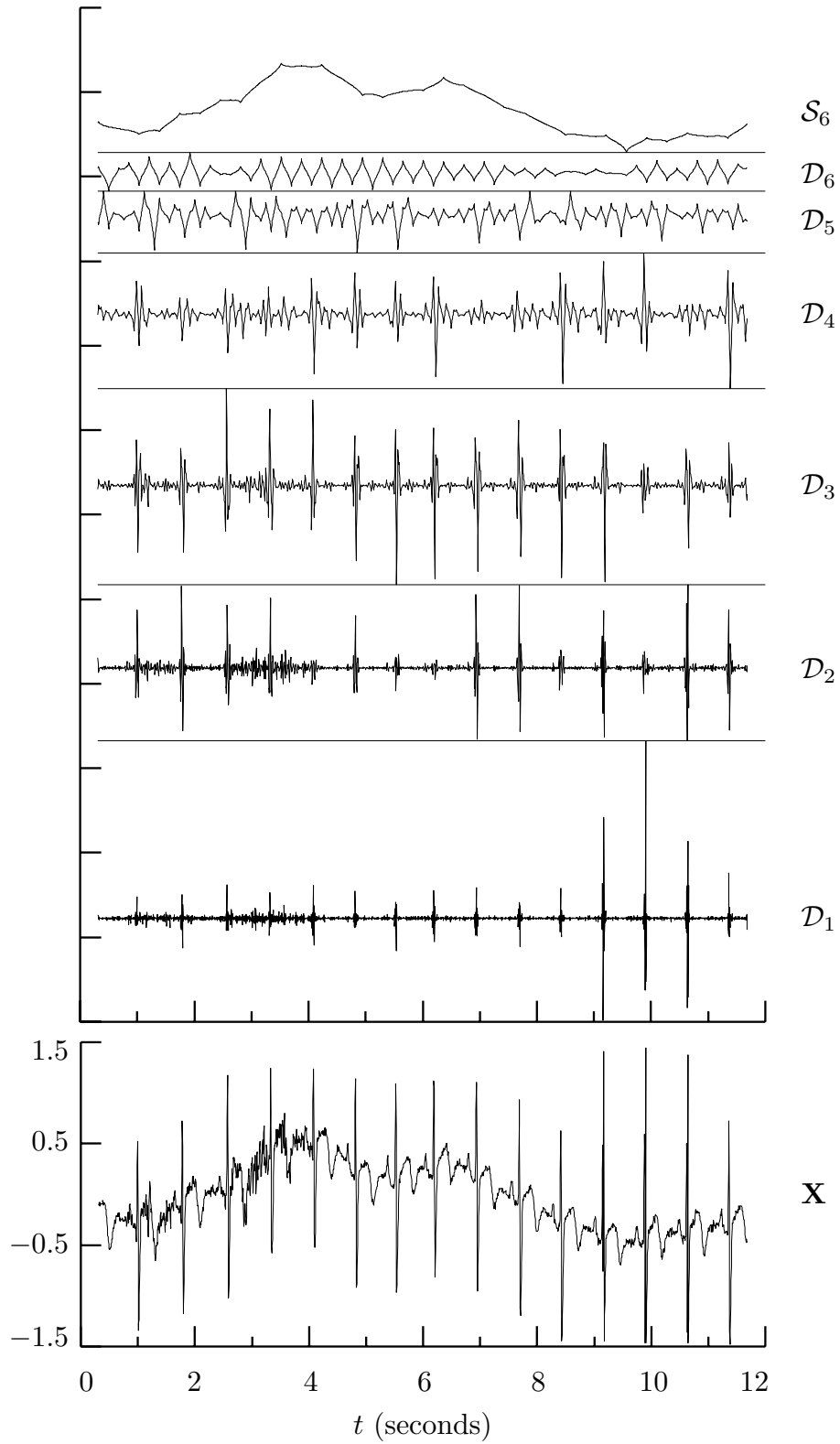
Figure 132. C(6) DWT multiresolution analysis of ECG time series (see text for details).
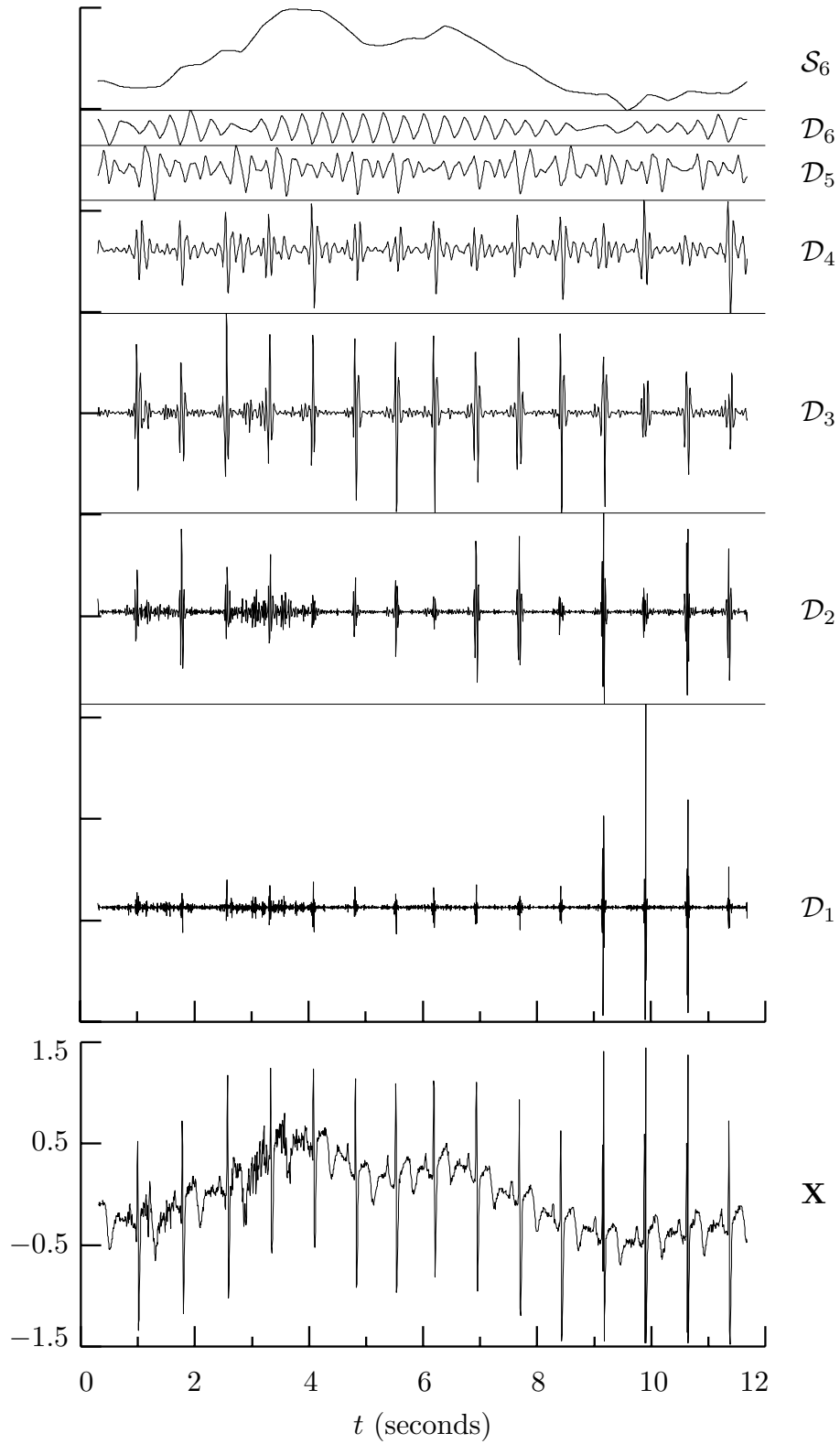
Figure 133. LA(8) DWT multiresolution analysis of ECG time series (see text for details).

L	L'_1	L'_2	L'_3	L'_4	$L'_{j\geq 5}$
2	0	0	0	0	0
4	1	2	2	2	2
6	2	3	4	4	4
8	3	5	6	6	6
10	4	6	7	8	8
12	5	8	9	10	10
14	6	9	11	12	12
16	7	11	13	14	14
18	8	12	14	15	16
20	9	14	16	17	18

Table 136. Number L'_j of boundary coefficients in $\mathbf{W}_j$ or $\mathbf{V}_j$ based on a wavelet filter of width L (here we assume $L'_j \leq N_j$, where $N_j = N/2^j$ is length of $\mathbf{W}_j$ or $\mathbf{V}_j$). The boundary coefficients are those that are influenced by boundary conditions at least to some degree.

L	$\bar{\gamma}_1^{(H)},\gamma_1^{(H)}$	$\bar{\gamma}_2^{(H)},\gamma_2^{(H)}$	$\bar{\gamma}_3^{(H)},\gamma_3^{(H)}$	$\bar{\gamma}_4^{(H)},\gamma_4^{(H)}$	$\bar{\gamma}_{j\geq5}^{(H)},\gamma_{j\geq5}^{(H)}$
8	1,2	3,2	3,3	3,3	3,3
10	2,2	3,3	4,3	4,4	4,4
12	2,3	4,4	5,4	5,5	5,5
14	2,4	4,5	6,5	6,6	6,6
16	3,4	6,5	7,6	7,7	7,7
18	4,4	6,6	7,7	8,7	8,8
20	4,5	7,7	8,8	9,8	9,9

Table 137a. Number of LA boundary wavelet coefficients at the beginning and the end of $\mathcal{T}^{-\gamma_j^{(H)}}\mathbf{W}_j$ (assuming $L_j' \leq N_j$). The number at the beginning is given by $\bar{\gamma}_j^{(H)}$, and the number at the end, by $\gamma_j^{(H)}$. Note that $\bar{\gamma}_j^{(H)} + \gamma_j^{(H)} = L_j'$, which is the total number of boundary coefficients (see Table 136).

L	$\bar{\gamma}_1^{(G)},\gamma_1^{(G)}$	$\bar{\gamma}_2^{(G)},\gamma_2^{(G)}$	$\bar{\gamma}_3^{(G)},\gamma_3^{(G)}$	$\bar{\gamma}_4^{(G)},\gamma_4^{(G)}$	$\bar{\gamma}_{J_0\geq5}^{(G)},\gamma_{J_0\geq5}^{(G)}$
8	2,1	3,2	4,2	4,2	4,2
10	2,2	3,3	3,4	4,4	4,4
12	3,2	5,3	5,4	6,4	6,4
14	4,2	6,3	7,4	8,4	8,4
16	4,3	6,5	7,6	8,6	8,6
18	4,4	6,6	7,7	7,8	8,8
20	5,4	8,6	9,7	9,8	10,8

Table 137b. As in Table 137a, but now for the LA scaling coefficients. Again we have $\bar{\gamma}_{J_0}^{(G)} + \gamma_{J_0}^{(G)} = L_{J_0}'$, where L_{J_0}' is given in Table 136.
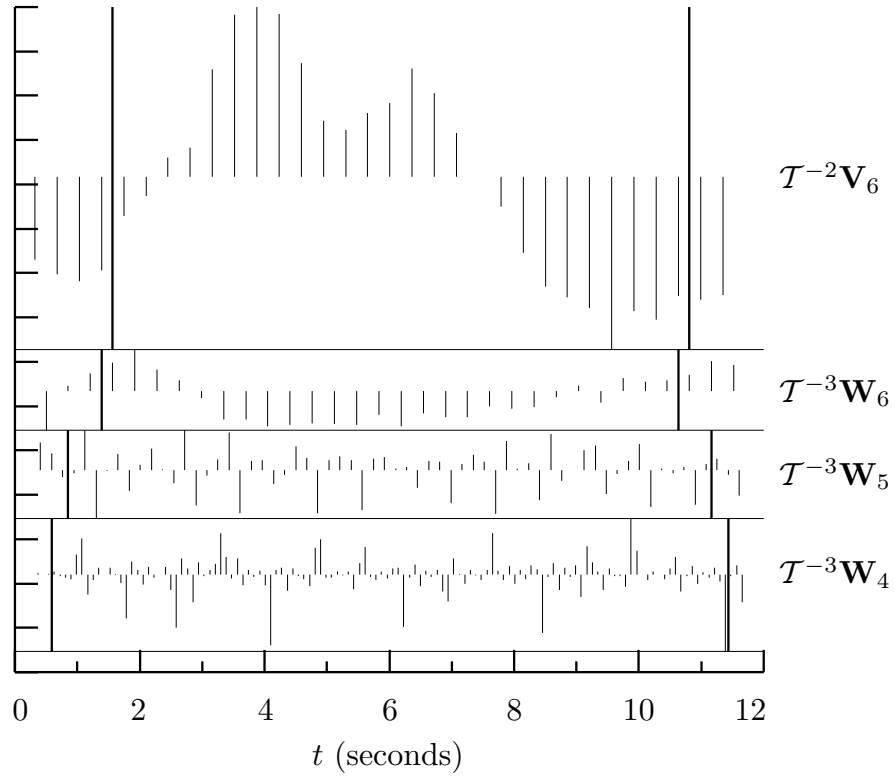
Figure 138. Four circularly advanced subvectors of the LA(8) DWT for the ECG time series (cf. Figure 127). The DWT coefficients plotted between the two thick vertical lines for a given subvector are unaffected by circularity, while those outside of the lines are the boundary coefficients. The number of plotted boundary coefficients agrees with the first rows of Tables 137a and 137b.
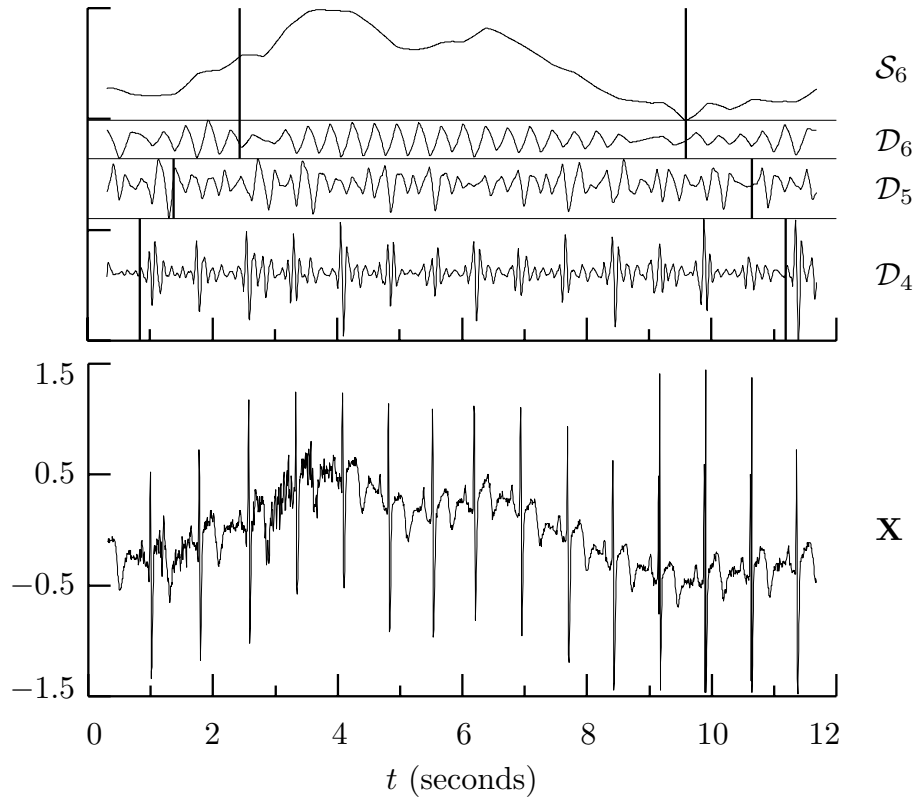
Figure 140. Portion of the LA(8) DWT multiresolution analysis for the ECG time series (the full analysis is shown in Figure 133). The thick vertical lines delineate the boundary regions in the details $\mathcal{D}_j$ and smooth $\mathcal{S}_6$ (i.e., those parts influenced to some degree by circularity).
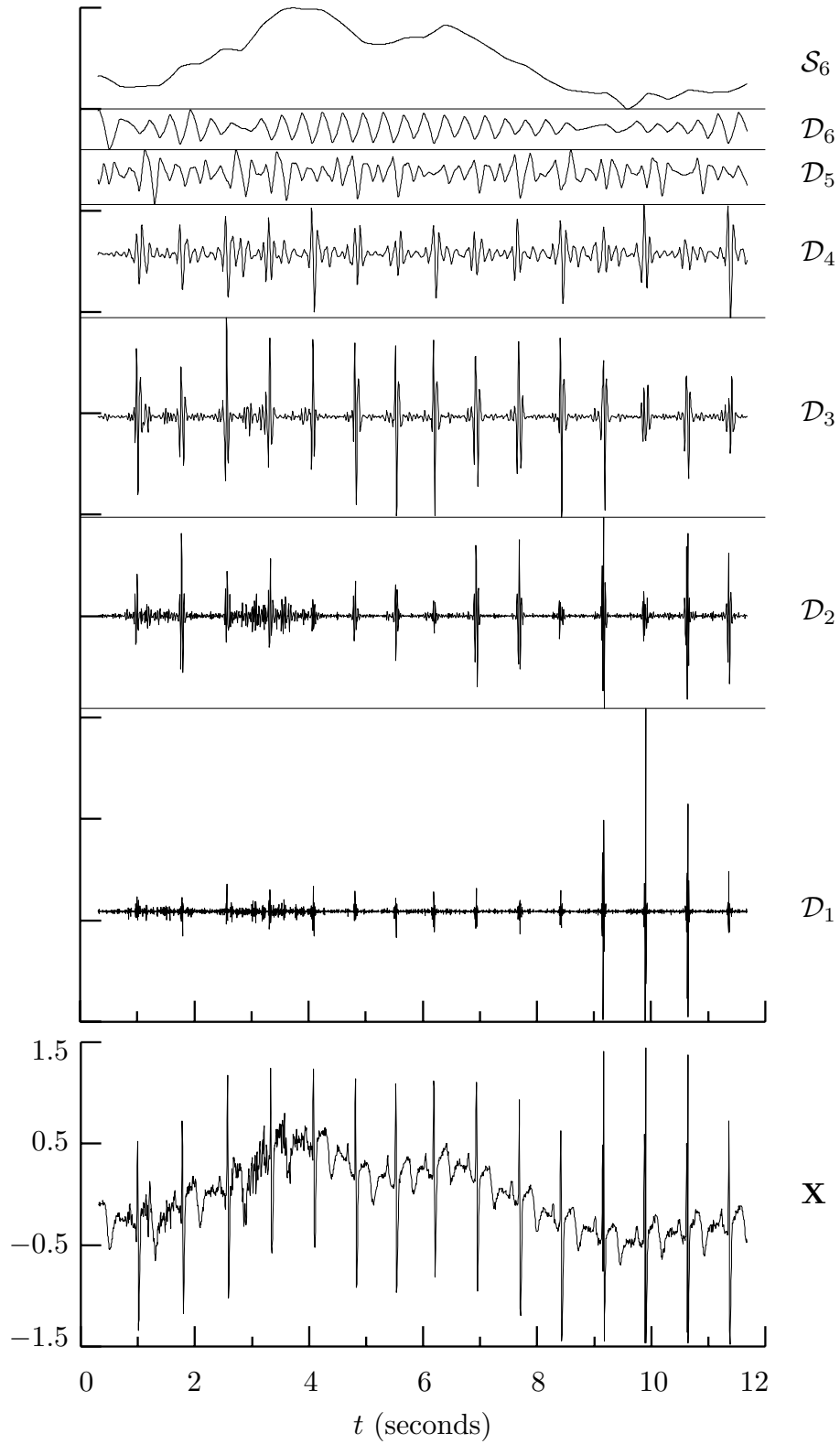
Figure 142. LA(8) DWT multiresolution analysis of ECG time series using reflection boundary conditions (cf. Figure 133).
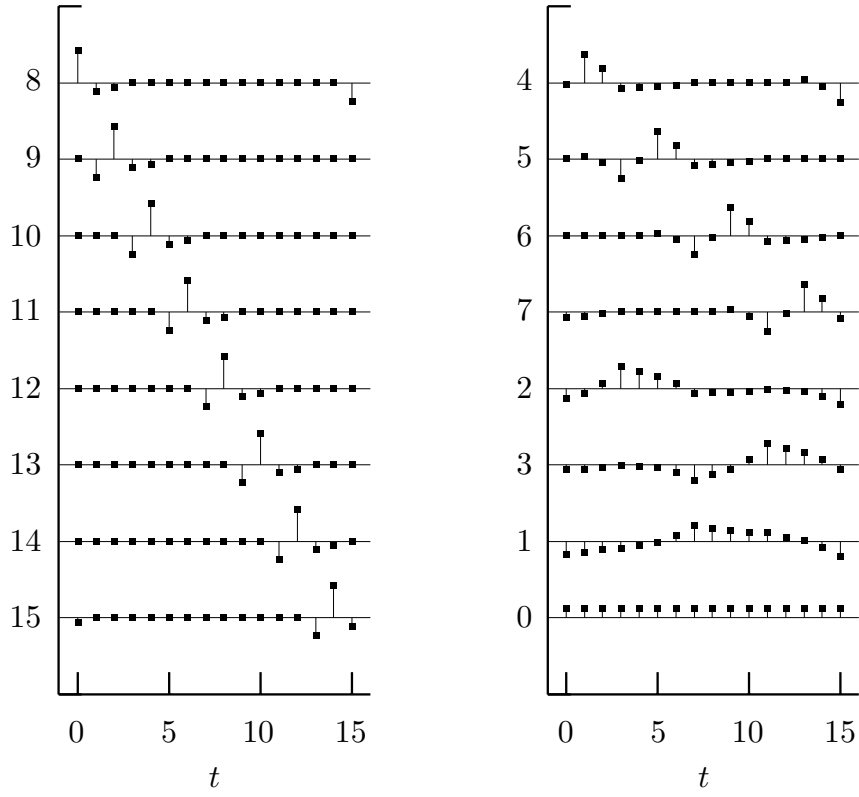
Figure 150. Row vectors of the discrete wavelet transform matrix based on the D(4) wavelet as defined in Bruce and Gao (1996a) – cf. Figure 60.

$$\{h_l\} \longleftrightarrow H(\cdot) \qquad\qquad \{g_l\} \longleftrightarrow G(\cdot)$$

$$h_l = (-1)^l g_{L-1-l} \qquad\qquad g_l \equiv (-1)^{l+1} h_{L-1-l}$$

$$H(f) = -e^{-i2\pi f(L-1)} G(\tfrac{1}{2} - f) \qquad G(f) = e^{-i2\pi f(L-1)} H(\tfrac{1}{2} - f)$$

$$\sum_l h_l = H(0) \equiv 0 \qquad\qquad \sum_l g_l = G(0) = \sqrt{2}$$

$$\sum_l h_l^2 \equiv 1 \qquad\qquad \sum_l g_l^2 = 1$$

$$\sum_l h_l h_{l+2n} \equiv 0, n \neq 0 \qquad \sum_l g_l g_{l+2n} = 0, n \neq 0$$

$$\sum_l g_l h_{l+2n} = 0$$

$$\mathcal{H}(f) \equiv |H(f)|^2 \qquad\qquad \mathcal{G}(f) \equiv |G(f)|^2$$

$$\mathcal{H}(f) + \mathcal{H}(f + \tfrac{1}{2}) = 2 \qquad \mathcal{G}(f) + \mathcal{G}(f + \tfrac{1}{2}) = 2$$

$$\mathcal{G}(f) + \mathcal{H}(f) = 2$$

$$W_{1,t} \equiv \sum_l h_l X_{2t+1-l \bmod N} \qquad V_{1,t} \equiv \sum_l g_l X_{2t+1-l \bmod N}$$

$$W_{j,t} \equiv \sum_l h_l V_{j-1,2t+1-l \bmod N_{j-1}} \qquad V_{j,t} \equiv \sum_l g_l V_{j-1,2t+1-l \bmod N_{j-1}}$$

$$h_{1,l} \equiv h_l, \;\; H_1(f) \equiv H(f) \qquad g_{1,l} \equiv g_l, \;\; G_1(f) \equiv G(f)$$

$$H_j(f) \equiv H(2^{j-1}f) \prod_{l=0}^{j-2} G(2^l f) \qquad G_j(f) \equiv \prod_{l=0}^{j-1} G(2^l f)$$

$$H_j(f) = H(2^{j-1}f) G_{j-1}(f) \qquad G_j(f) = G(2^{j-1}f) G_{j-1}(f)$$

$$\{h_{j,l}\} \longleftrightarrow H_j(\cdot) \qquad\qquad \{g_{j,l}\} \longleftrightarrow G_j(\cdot)$$

$$\sum_l h_{j,l} = H_j(0) = 0 \qquad\qquad \sum_l g_{j,l} = G_j(0) = 2^{j/2}$$

$$\sum_l h_{j,l}^2 = 1 \qquad\qquad \sum_l g_{j,l}^2 = 1$$

$$\sum_l h_{j,l} h_{j,l+2^j n} = 0, n \neq 0 \qquad \sum_l g_{j,l} g_{j,l+2^j n} = 0, n \neq 0$$

$$\sum_l g_{j,l} h_{j,l+2^j n} = 0$$

$$\mathcal{H}_j(f) \equiv |H_j(f)|^2 \qquad\qquad \mathcal{G}_j(f) \equiv |G_j(f)|^2$$

$$W_{j,t} = \sum_l h_{j,l} X_{2^j(t+1)-1-l \bmod N} \qquad V_{j,t} = \sum_l g_{j,l} X_{2^j(t+1)-1-l \bmod N}$$

Table 154. Key relationships involving wavelet and scaling filters. Because $h_l = g_l = 0$ for all $l < 0$ and $l \geq L$, summations involving h_l or g_l can be taken to range from either $l = 0$ to $l = L - 1$ or over all integers; likewise, summations involving $h_{j,l}$ or $g_{j,l}$ can range either from $l = 0$ to $l = L_j - 1$ or over all integers (recall that $L_j \equiv (2^j - 1)(L - 1) + 1$ and that $N_j \equiv N/2^j$).